State of Oregon
Oregon Department of Geology and Mineral Industries
Ruarri J. Day-Stirrat, State Geologist

OPEN-FILE REPORT O-24-11

IMPROVED CASCADIA EARTHQUAKE SOURCE MODELS FOR TSUNAMI HAZARD ASSESSMENT

By Matthew Sypus and Kelin Wang[1]

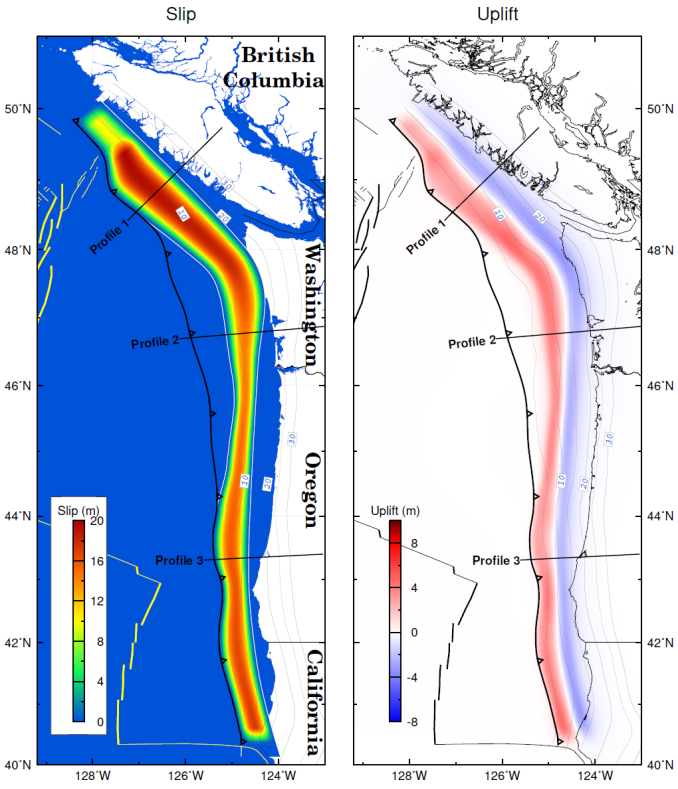

2024

[1]School of Earth and Ocean Sciences, University of Victoria, PO Box 1700 STN CSC, Victoria BC V8W 2Y2, Canada

DISCLAIMER

This product is for informational purposes and may not have been prepared for or be suitable for legal, engineering, or surveying purposes. Users of this information should review or consult the primary data and information sources to ascertain the usability of the information. This publication cannot substitute for site-specific investigations by qualified practitioners. Site-specific data may give results that differ from the results shown in the publication.

WHAT'S IN THIS REPORT?

This report describes the development of a suite of new Cascadia Subduction Zone (CSZ) megathrust source scenarios. Compared to previous Cascadia tsunami source models, several improvements are made. These improvements have been aided by the recent release of new data from the Cascadia Seismic Imaging Experiment 2021 (CASIE21), reinterpreted legacy seismic data, seismicity, and low-frequency earthquakes (LFE) in Episodic Tremor and Slip (ETS) events.

Cover: A full margin megathrust earthquake, assuming 500 years of plate convergence, highlighting both earthquake slip (left) and along-coast vertical deformation (right).

Oregon Department of Geology and Mineral Industries Open-File Report O-24-11
Published in conformance with ORS 516.030

For additional information:
Administrative Offices
800 NE Oregon Street, Suite 965
Portland, OR 97232
Telephone (971) 673-1555
https://www.oregongeology.org
https://oregon.gov/DOGAMI/

The study benefitted from essential contributions from the following groups and many other scientists working on understanding Cascadia seismic and tsunami hazards.

The Cascadia Sources Working Group (CSWG): Matthew Sypus, Kelin Wang, and Yijie Zhu (University of Victoria), Hong Kie Thio (AECOM), Jonathan Allan and Reed Burgette (DOGAMI), Chris Goldfinger (Oregon State University), Stephanie Ross and Janet Watt (USGS), Jason R. Patton (California Geological Survey), Harold Tobin, Anna Ledeczi, and Madeleine Lucas (University of Washington), Corina Allen, Daniel Eungard, and Alex Dolcimascolo (Washington Department of Natural Resources).

The CASIE21 team, especially Suzanne Carbotte (LDEO, Columbia University), Juan Pablo Canales (Woods Hole Oceanographic Institution), and Shuoshuo Han (University of Texas, Austin).

The ad hoc Working Group for Synthesizing Legacy Seismic Data for Southern Cascadia off of California: Anne Tréhu (Oregon State University) and other colleagues, including Sean Gulick (University of Texas, Austin) and Brandon Shuck (LDEO, Columbia University).

TABLE OF CONTENTS

Executive Summary **1**

1.0 Introduction **2**

2.0 Improved Cascadia Fault Geometry **3**

2.1 New Model of the Megathrust Geometry 3
2.2 Splay-Faulting Rupture 11
2.3 Frontal Thrust and Trench-Breaching Rupture 11

3.0 Modelling Method **14**

3.1 3D Dislocation Model 14
3.2 Effects of Sloping Seafloor in a Flat-Surface Model 14
3.3 Constructing 3D Fault Mesh 21
3.4 Assigning Slip Vectors 22

4.0 Overview of Cascadia Tsunami Source Scenarios **24**

5.0 Whole-Margin Rupture Scenarios **32**

5.1 Whole-Margin Buried Rupture 32
5.2 Whole-Margin Splay-Faulting Rupture 38
5.3 Whole-Margin Trench-Breaching Rupture 40
5.4 Asperity Models 42

6.0 Partial Rupture Scenarios **43**

6.1 Segmented Tsunami Source Models 43
6.2 Cluster M8 Tsunami Source Models 47
6.3 Floating Tsunami Source Models 47

7.0 Conclusion **52**

8.0 Acknowledgments **53**

9.0 References **54**

10.0 Appendix A **58**

LIST OF FIGURES

Figure 1.1. Earthquake rupture types used in this study. 3

Figure 2.1. A) CASIE21 profile line names. Black, blue, purple, and red seismic profile lines have both the top of crust (TOC) and shallower plate boundary (SPB) interpreted 5
Figure 2.2. Plate boundary geometry along CASEI21 profiles shown in Figure 2.1 6
Figure 2.3. Comparison of the new Cascadia megathrust geometry used in this study (red contours) with previous geometries (gray contours) 10
Figure 2.4. Traces of the two assumed splay faults used for modelling. Splay B (or “extended L1”) is shown in blue and the new Splay D trace is in green 12
Figure 2.5. Information regarding the frontal thrust geometry 13

Figure 3.1. Adjustments to fault geometry in models with a flat top (from Sypus, 2019) 15
Figure 3.2. Trench-breaching (left) and buried (right) rupture examples to show the effectiveness of the fault dip adjustment shown in Figure 3.1, with uniform rigidity (any value) and Poisson’s ratio (0.25) 16

Figure 3.3. Bathymetry and fault dip adjustment 17
Figure 3.4. Profiles showing how the new geometry, water-adjusted geometry, trench-breaching geometry, and splay-faulting geometries and bathymetry relate 18
Figure 3.5. Construction of fault mesh in the dislocation model 21
Figure 3.6. Normalized slip in the margin normal direction 23
Figure 3.7. Illustration of how the special up-skewed buried rupture (black solid line in (B)) off Washington (green area in Figure 2.5b is constructed. 23
Figure 3.8. Schematic illustration of how slip magnitude scales with local rupture zone width 24

Figure 4.1. Logic tree for a whole margin and partial CSZ rupture constructed by the USGS-NTHMP Cascadia Powell Center Tsunami Sources Working Group and updated by the CSWG. 25
Figure 4.2. Illustration of the two whole-margin (A and A+Exp) models and the along-strike definition of the segmented ruptures 30
Figure 4.3. Map showing the main dip direction rupture boundaries 31

Figure 5.1. Examples of the slip of distribution (upper panels) and surface vertical deformation (lower panels) of whole-margin A) deep and B) shallow buried rupture 33
Figure 5.2. Surface deformation, fault slip and fault for profiles 1 to 3 (from north to south) in Figure 5.1, showing results for deep (black lines) and shallow (red lines) whole margin buried rupture scenarios. 34
Figure 5.3. Examples of the slip of distribution (upper panel) and vertical deformation (lower panel) of whole-margin (A) up-skew, (B) symmetric, and (C) down-skew buried rupture 35
Figure 5.4. Surface deformation, fault slip, and fault geometry for profiles 1 to 3 (from north to south) in Figure 5.3, showing results for up-skew (red lines), symmetric (black lines), and down-skew (blue lines) whole margin shallow buried scenarios 36
Figure 5.5. Examples of the slip of distribution (upper panel) and vertical deformation (lower panel) of whole-margin buried rupture 37
Figure 5.6. Surface deformation, fault slip, and fault geometry for profiles 1 to 3 (from north to south) in Figure 5.5, showing results for the Midpoint locked and 1 cm locked (M, red lines), Locked zone (L, green lines) and Tremor (T, purple lines) downdip limits. 38
Figure 5.7. Examples of the slip of distribution (upper panel) and vertical deformation (lower panel) from the whole-margin splay-faulting rupture for (A) Splay B and (B) Splay D 39
Figure 5.8. Surface deformation, fault slip, and fault geometry for profiles 1 to 3 (from north to south) in Figure 5.7 40
Figure 5.9. Examples of whole-margin trench-breaching scenarios, including the area that lacks evidence for seaward vergence faulting off of the Washington coast 41
Figure 5.10. Surface deformation, fault slip, and fault geometry for profiles 1 to 3 (from north to south) in Figure 5.9 42
Figure 5.11. Examples of the DOGAMI whole-margin n = 3 asperity models 44
Figure 5.12. Illustration of the along-strike variations of slip in the five USGS asperity models 45
Figure 5.13. Examples of the whole-margin n = 5 asperity models 46

Figure 6.1. Definition of the five-level cluster ruptures based on the cluster setup in the USGS NSHM. 48
Figure 6.2. Examples of the five-level cluster ruptures 49
Figure 6.3. Floating rupture boundaries 50
Figure 6.4. Slip distribution (upper) and surface vertical deformation (lower) for all ten elliptical floating-rupture patch scenarios 51

LIST OF TABLES

Table 4.1. Naming convention for Cascadia tsunami sources. 28

ACCOMPANYING MODEL DATA

This report is accompanied by the following data:

Geophysical model data: *The accompanying* ***O-24-11_model_data.zip*** *file contains a comprehensive update and refinement of tsunami source scenarios for the Cascadia subduction zone, incorporating a suite of 3,502 models developed by integrating new CASIE21 seismic imaging data, updated geological interpretations, and advanced modeling techniques.*

Geometry data: *The accompanying* ***O-24-11_geometry_data.zip*** *file contains additional information used to construct the various rupture scenarios provided as part of this report. The zip file includes 5 different geometry files: 1. The main geometry; 2. The adjusted buried geometry after subtracting out water depth; 3. The trench breaching geometry; 4. Splay B geometry file; and finally, 5. Splay D geometry. Both splay and trench breaching geometries are modified from the buried geometry that has water depth subtracted.*

EXECUTIVE SUMMARY

This report describes the approaches used to construct megathrust source scenarios by integrating multiple datasets, the overarching goal being the eventual development of new probabilistic tsunami hazard analyses for Cascadia. Compared to previous Cascadia tsunami source models, several improvements are made. The megathrust geometry model is much improved, owing mainly to new data from the Cascadia Seismic Imaging Experiment 2021 (CASIE21). Constraints in addition to the depth of CASIE21 imaging presently include earlier seismic surveys, seismicity, and low-frequency earthquakes (LFE) in Episodic Tremor and Slip (ETS) events. Offshore of northern California, which was not imaged by CASIE21, the geometry is constrained by reinterpreted legacy seismic data and seismicity. In the downdip direction, we include three main types of rupture scenarios: buried rupture, splay faulting rupture, and trench-breaching rupture. In all cases, the downdip rupture limits are the same as assumed in the USGS National Seismic Hazard Model. CASIE21 imaging, combined with high-resolution sparker imaging, does not support the interpretation of the presence of a continuous active mega-splay fault along the margin, although these data yield limited evidence to allow a hypothetical mega splay from 43°N–47°N, which will likely have some implications for tsunami hazard in Washington state and British Columbia. To comply with local geological evidence, we incorporate Holocene turbidite, estuary, and lake records, and known structural heterogeneity to guide the design of rupture lengths and recurrence intervals. Finally, to account for aleatoric uncertainties, we also construct random rupture scenarios that are not based on geologic evidence.

1.0 INTRODUCTION

The Cascadia Subduction Zone (CSZ) that extends from offshore of California to British Columbia has generated great earthquakes with large tsunamis. Various predictive earthquake rupture scenarios have been constructed in the past for assessing tsunami hazards by different states along the west coast and by the American Society of Civil Engineers (ASCE) for building code regulations. Towards developing a new U.S. national probabilistic tsunami hazard assessment (PTHA) model for Cascadia, a Powell Center meeting dedicated to Cascadia rupture sources was held in Fort Collins, Colorado on May 9 to 13, 2022, drawing together scientific experts in paleoseismology, Cascadia geophysics, earthquake fault mechanics, geology, and hydrodynamic modeling (Patton and others, 2022). The workshop and subsequent discussion led to the development of an updated earthquake/tsunami logic tree for developing the new PTHA model.

In December 2022, with the goal of constructing improved Cascadia source scenarios guided by the updated logic tree, an interagency agreement was initiated between the Oregon Department of Geology and Mineral Industries (DOGAMI) and the University of Victoria. This report describes the construction of 3,502 source scenarios under this initiative. Over the ensuing 14 months, we held numerous meetings and discussion sessions with many Cascadia scientists. Their collective input provided valuable guidance. We refer to those who more regularly joined the discussion meetings as the Cascadia Sources Working Group (CSWG). Our preliminary results were reported at the 2024 American Geophysical Union Fall meeting (Sypus and others, 2023), and feedback from others working on tsunami hazard along the Cascadia margin was very useful to the completion of these scenarios.

Combining interpretations of newly available controlled-source seismic imaging results and other types of information, as described in Section 2, we developed an updated model geometry of the megathrust and secondary faults needed for these updated tsunami source scenarios. For most of Cascadia, except off of the California coast, the CASIE21 data have allowed further constraints of shallow geometry from the deformation front down to about 15 km depth. The geometry is also informed by previously used legacy seismic imaging data, intraslab earthquake locations, and depth locations of LFE that occur during ETS events.

To fulfill the needs of the PTHA, we provide a suite of rupture scenarios that vary in rupture type, downdip extent, along strike extent, and in localization of peak slip. Where possible, relevant parameters, particularly those defining rupture dimension, are chosen to be compatible with the existing U.S. national seismic hazard model (NHSM). The three types of ruptures considered in this study include buried, trench-breaching, and splay-faulting ruptures following Gao and others (2018), as schematically illustrated in **Figure 1.1**. Accommodating the presence of thick sediment burying the trench at Cascadia, our trench-breaching scenarios include the activation of a frontal thrust (Gao and others, 2018) in areas where there is evidence for the presence of seaward-vergent faults at the toe of the accretionary prism. In areas without evidence for such seaward-vergent faults, we apply an updip-skewed buried slip distribution, approximately representing the effect of plastic deformation of the outer accretionary wedge (Ma, 2012).

This report is focused on the operational aspect of the construction of the source scenarios. The various decisions and choices of parameters in this study are based on not only discussions with the CSWG and the broader Cascadia research community but also a large range of geodynamic arguments on the basis of subduction zone tectonics, knowledge learned from tsunamigenic earthquakes in other subduction zones, and principles of fault mechanics. The science behind these arguments is summarized in an article

by Wang and others (2024). Theoretical justifications for the various model simplifications and assumptions invoked in this study are provided in a paper by Zhu and others (in preparation).

Figure 1.1. Earthquake rupture types used in this study.

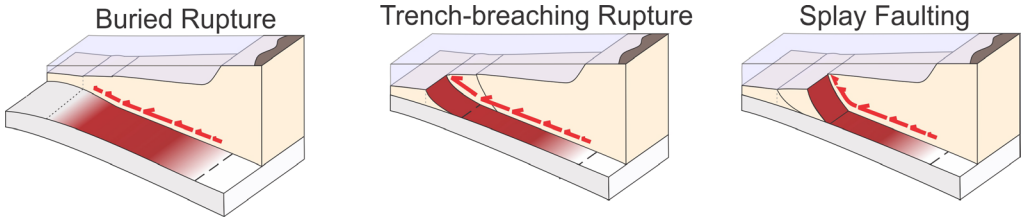

2.0 IMPROVED CASCADIA FAULT GEOMETRY

2.1 New Model of the Megathrust Geometry

We constructed the new model of the Cascadia megathrust (**Figure 2.1**) by synthesizing four types of information: (1) data from the CASIE21, (2) hypocenter locations of LFEs, (3) legacy controlled-source seismic data collected in the 1980's and 1990's, and (4) intraslab earthquake hypocenter locations. We directly used the CASIE21 data (e.g., Carbotte and others, 2024) to constrain the shallow part of the megathrust and LFE data to inform its 30 km–40 km depth range. The comparison of the model geometry with the CASIE21 and LFE data is shown in **Figure 2.2** for all the CASIE survey lines.

CASIE21 is a recent multichannel seismic experiment conducted using a 12-km- to 15-km-long receiver array collecting ~5,500 km of data covering offshore Oregon, Washington, and British Columbia (**Figure 2.1a**) (Carbotte and others, 2024). The CASIE21 experiment has provided unprecedented spatial coverage and resolution of the shallow geometry of megathrust north of California. The CASIE21 team interpreted their seismically imaged horizons of the top of the subducting igneous crust (TOC) and, in some profiles, a shallower horizon identified as the décollement, separating sections of subducted and accreted sediment. Where there is no evidence for significant sediment subduction, the TOC is assumed to be the megathrust horizon. Where there is sediment subduction, the décollement is assumed to be the megathrust. We assume smooth transitions between these areas because an abrupt change would require faulting for which no geological evidence is available. Various complex features were found in the CASIE21 profiles (**Figure 2.1**) such as deep sediment underthrusting (profiles: PD05, PD06, PS06, TD08D06, TD05D07, TD08D06), shallow sediment underthrusting (profiles: PD12, PD13, PD14, PD15, PD16, PD17, and PD18), and a significant offset of the subducting crust in the strike direction near 47°N (profiles: TD08D06 and PS01ACD). See Carbotte and others (2024) for a more detailed description of the imaged structure.

The CASIE21 team kindly provided picks of the TOC and the décollement from their depth-migrated seismic images prior to final publication. We first created TOC depth contours to fit the TOC picks to achieve a smoothed geometry for the top of crust. We then modified this geometry wherever necessary by fitting the décollement picks along individual margin-normal profiles, including the CASIE21 survey lines. Thus, the resulting megathrust geometry represents the TOC in some places and the décollement in other places. For example, off of Oregon (42.5°N to 44.5°N), up to about 2.5 km of the lower sediment layer is being subducted, resulting in a shallower megathrust in this area. Compared to the more detailed interpretation of Carbotte and others (2024), our megathrust geometry is smoother (**Figure 2.2**). This modified geometry reflects the tendency of a natural, mature fault to gain a smoother geometry through

shearing (e.g., Wang and Bilek, 2014). This smoothing is within the range of depth uncertainties from interpretation of the imaging results.

Where the LFE data are available (**Figure 2.1b**), they help constrain a deeper part of the megathrust than what the CASIE21 data could cover. Various types of studies, including receiver functions, tomographic analyses, and earthquake relocations have been used to understand the deeper geometry of the subducting slab at Cascadia. They have yielded contradictory and controversial results due to ambiguities in interpreting imaged seismic discontinuities, inadequate spatial resolution of tomographic images, and not knowing exactly in which part of the slab the intraslab events occur. We adopt the commonly agreed upon interpretation that the LFEs occur along the megathrust during ETS around the mantle wedge corner (e.g., Gomberg and others, 2010; Gao and Wang, 2017, and references therein). The simplicity of this interpretation makes the LFE data useful to constrain the megathrust interface location for this depth range. There is still some scatter in LFE depths due to location errors.

When manually constructing a smooth geometry, we let the megathrust run through the approximate average depth of the data scatter while maintaining a simple curvature of the slab in both the dip and strike directions (**Figure 2.2**). Four sets of LFE data were used, including those for Northern Vancouver Island (Savard and others, 2020; Merrill and others, 2022), Southern Vancouver Island (Savard and others, 2018), Washington (Royer, 2014), and Northern California (Plourde and others, 2015). Where no good-quality LFE data have been reported in Oregon (between ~42°N to 47°N), the deeper geometry depends heavily on earlier models as explained in the next paragraph.

The use of the legacy controlled-source seismic data and intraslab earthquake data was indirect. Earlier studies such as Flück and others (1997), McCrory and others (2006, 2012), and Hayes and others (2018) used these data to constrain Cascadia megathrust geometry. Gao and others (2018) and Sypus (2019) synthesized the earlier geometry models by smoothly connecting depth contours from McCrory and others (2006) and Gao and others (2017) for central and northern Cascadia, and those by McCrory and others (2012) and Hayes and others (2018) for southern Cascadia. By incorporating much of the information from Gao and others (2018) and Sypus (2019), our new model indirectly inherits the constraints provided by the legacy controlled-source seismic data and intraslab earthquake data, especially for areas not covered by CASIE21, such as offshore of California and greater than about 20 km depth anywhere along the margin.

For offshore of California, the ad hoc Working Group for Synthesizing Legacy Seismic Data for Southern Cascadia off of California revisited the 1994 Mendocino Triple Junction Seismic Experiment (MTJSE) (Beaudoin and others, 1996) and other relevant data (e.g., Gulick and others, 1998). Their newly delineated shallow geometry of the megathrust in this region (**Figure 2.1b**) differs from, and appears to be somewhat a compromise of, those previously published in the two studies by McCrory and others (2006, 2012) based on intraslab earthquake locations and regional seismic velocity studies. The new model portrays a downward deflection of the subducting slab just to the north of the Mendocino Triple Junction (MTJ), but not as pronounced as in McCrory and others (2012). For areas outside the MTJSE coverage and not re-examined by Tréhu and others (personal communications, 2023) the earlier results between McCrory and others (2006) and McCrory and others (2012) are similar, and we continue to use these results.

Figure 2.1. A) CASIE21 profile line names. Black, blue, purple, and red seismic profile lines have both the top of crust (TOC) and shallower plate boundary (SPB) interpreted. Thin lines extending from the margin-normal profiles are used to constrain the geometry. Gray lines only have a TOC interpreted horizon. B) Controls for creating a TOC geometry include data from CASIE21 (Carbotte and others, 2024), LFEs (Royer and Bostock, 2014; Plourde and others, 2015; Savard and others, 2018; Savard and others, 2020), and shallow depth contours (red) near the Mendocino Triple Junction provided by Tréhu and others (personal communications, 2023). C) Megathrust geometry model, shown as depth contours, created for this report. Colored depth controls of the shallower interface interpreted from CASIE21 images.

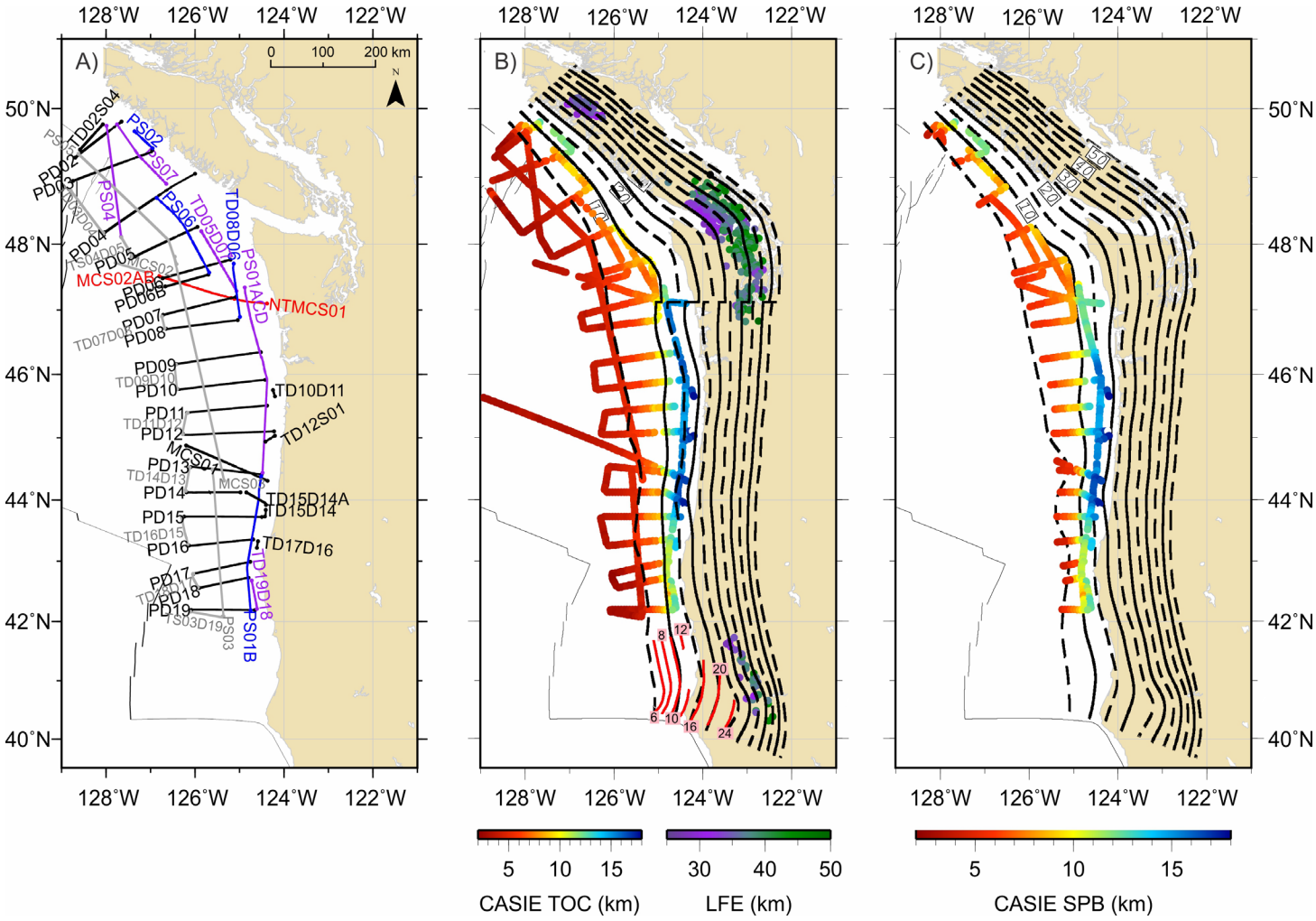

Figure 2.2. Plate boundary geometry along CASEI21 profiles shown in Figure 2.1. Blue and orange dots are interpreted as depth of the TOC and shallower sedimentary décollement, respectively (Carbotte and others, 2024). Darker blue and brown dots are projected from interpreted depths using crossing profiles. Red dots are LFEs (Royer, 2014; Plourde and others, 2015; Savard and others, 2018; Savard and others, 2020).

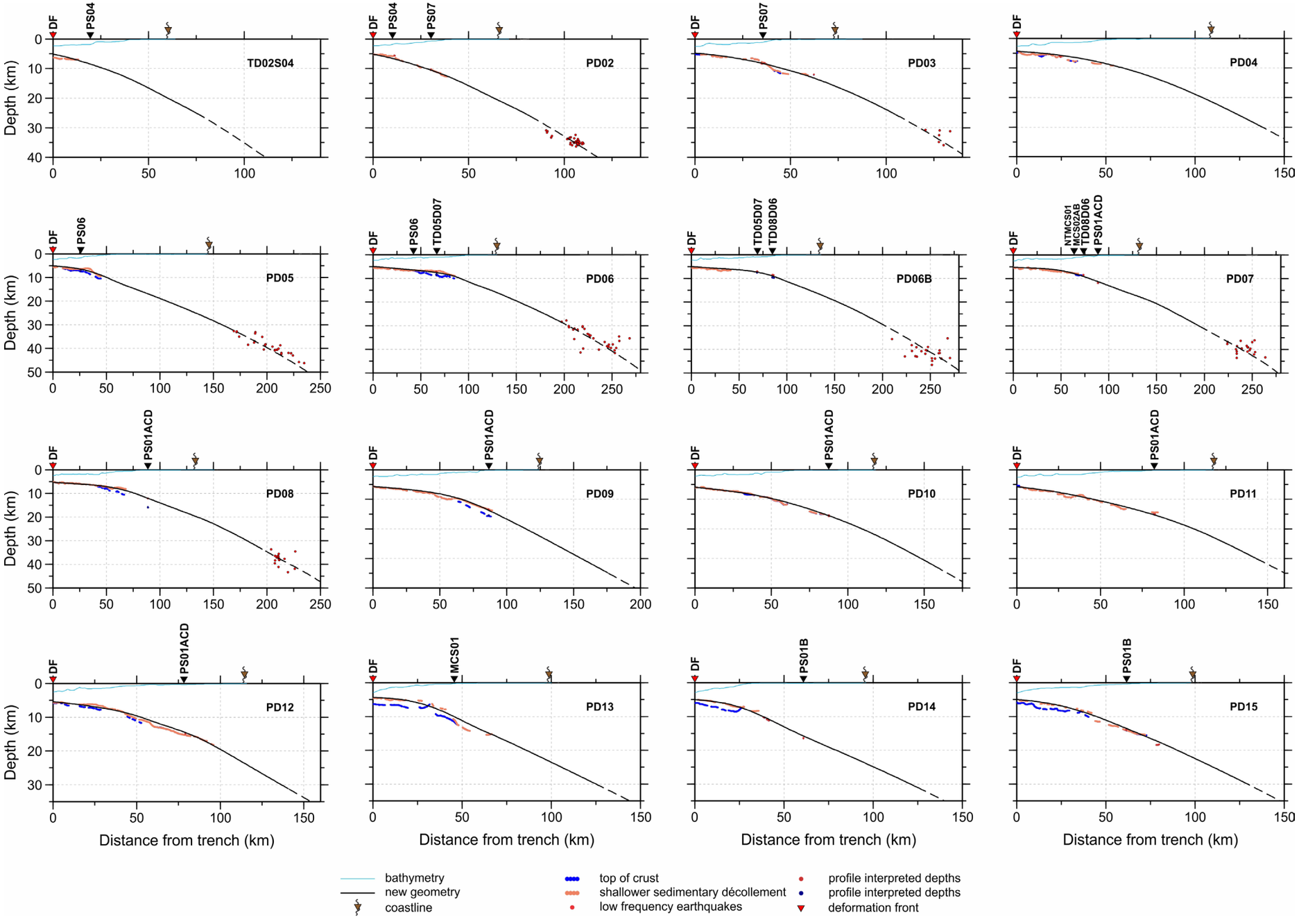

Figure 2.2 (cont.). Plate boundary geometry along CASEI21 profiles shown in Figure 2.1. Blue and orange dots are interpreted as depth of the TOC and shallower sedimentary décollement, respectively (Carbotte and others, 2024). Darker blue and brown dots are projected from interpreted depths using crossing profiles. Red dots are LFEs (Royer, 2014; Plourde and others, 2015; Savard and others, 2018; Savard and others, 2020).

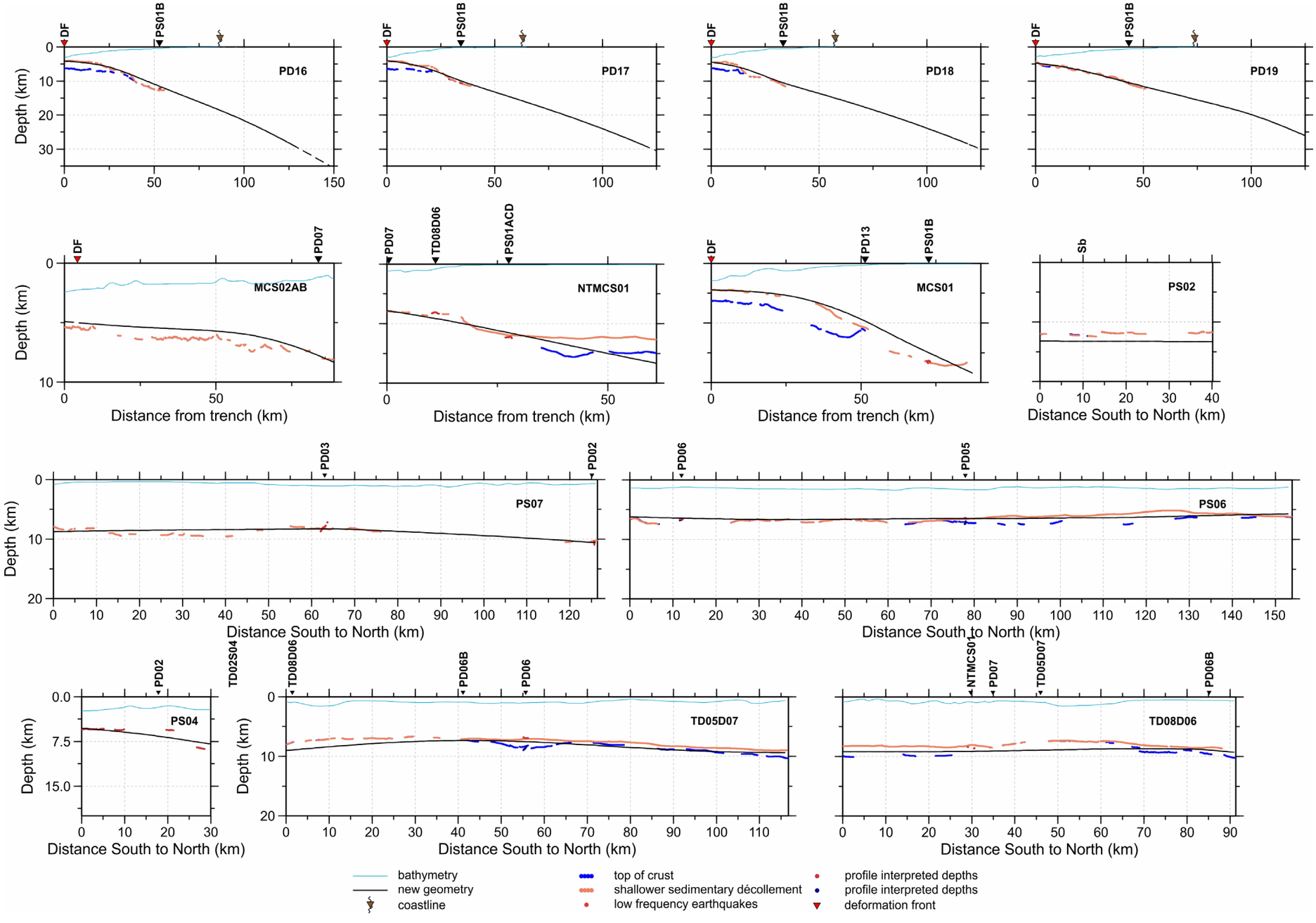

Figure 2.2 (cont.). Plate boundary geometry along CASEI21 profiles shown in Figure 2.1. Blue and orange dots are interpreted as depth of the TOC and shallower sedimentary décollement, respectively (Carbotte and others, 2024). Darker blue and brown dots are projected from interpreted depths using crossing profiles. Red dots are LFEs (Royer, 2014; Plourde and others, 2015; Savard and others, 2018; Savard and others, 2020).

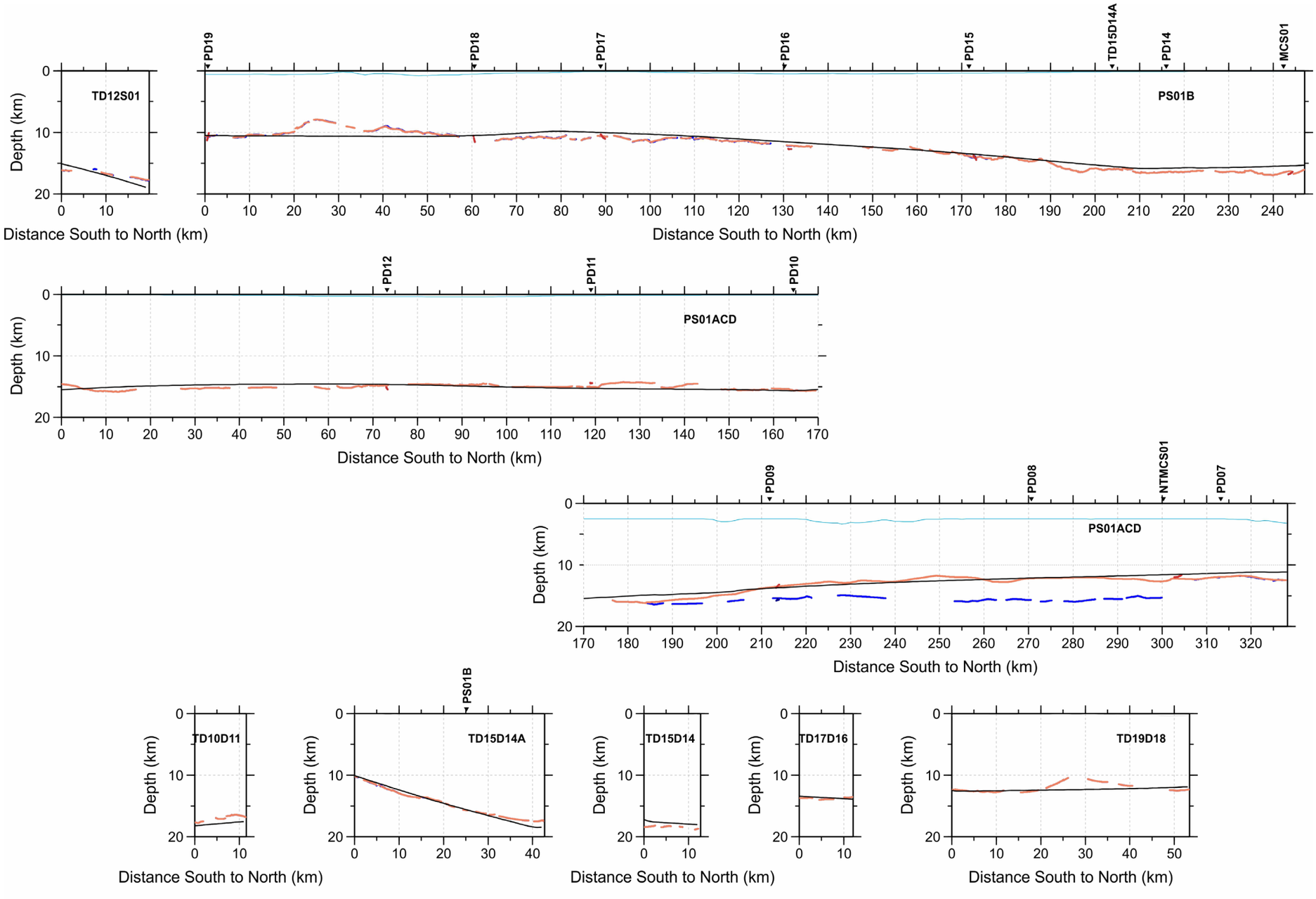

Where there is overlap in data coverage, there are often strong similarities between the geometry published in earlier studies and the new findings from CASIE21 and LFE pick locations (**Figure 2.3**). This adds great confidence in stitching together a megathrust model based on the four types of constraints. Taking into account mechanical considerations regarding the nature of fast-moving faults and the uncertainties within the data, we have constructed a megathrust model that is smoother than the geometry initially constrained simply from depth data (such as the CASIE21 picks). The geometry model created in this study is thus a compromise that avoids potentially spurious anomalies that could influence tsunami modeling in unrealistic ways. Comparisons of the new model with earlier models are shown in **Figure 2.3**.

Figure 2.3. Comparison of the new Cascadia megathrust geometry used in this study (red contours) with previous geometries (gray contours) for which the reference is given at the top. Dashed and solid lines are the 5 km and 10 km increment contours, respectively.

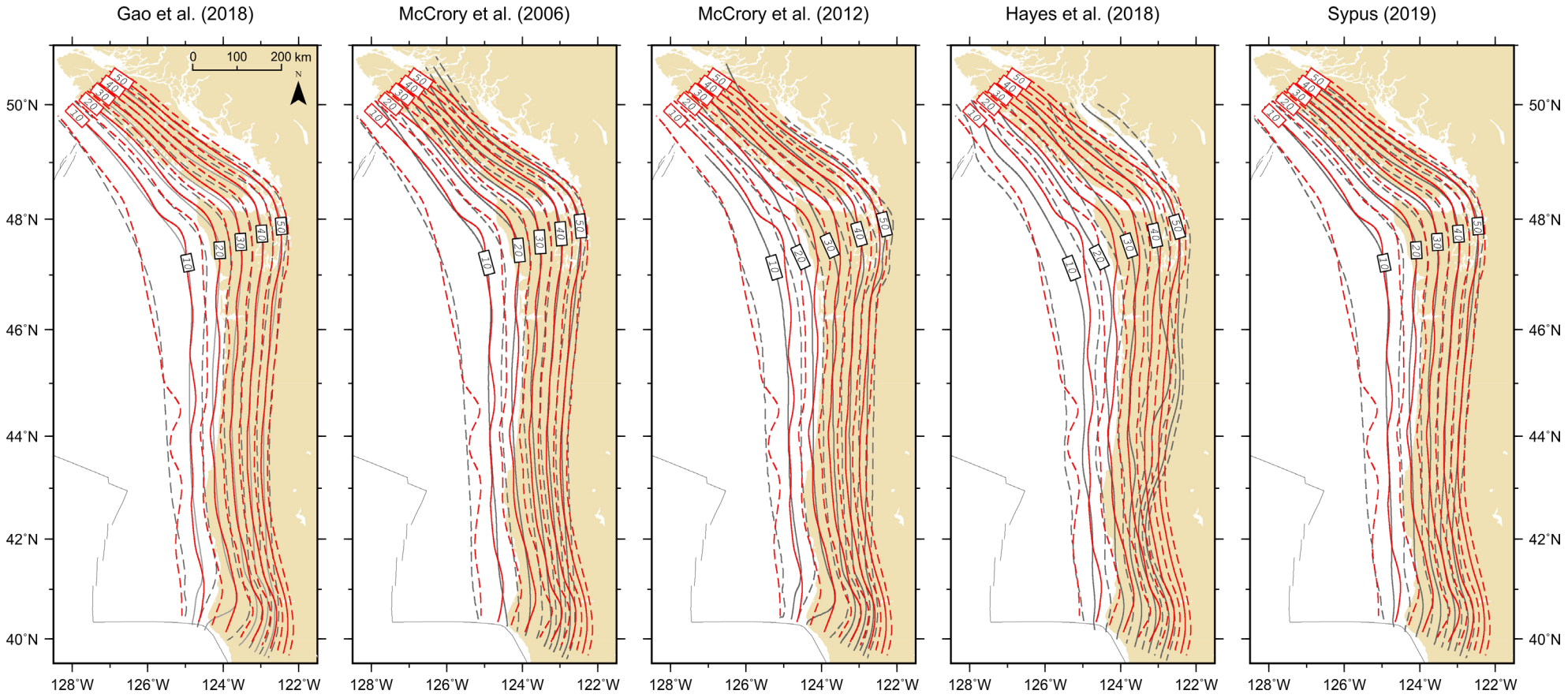

2.2 Splay-Faulting Rupture

The construction of a splay fault (**Figure 1.1**) involves manually assigning control points to connect the megathrust to a more steeply dipping thrust fault that breaks the seafloor. **Figure 2.4** shows the traces of two hypothesized splay faults, named Splay B (blue line) and Splay D (green line), considered in this study. As explained below, the confidence of the research community in the presence, continuity, and/or present activity of the splay faults is much reduced owing to the CASIE21 imaging, although the confidence in Splay D is higher than in Splay B.

The surface trace of Splay B (and its naming) is from Gao and others (2018), but its dip is steeper than in Gao and others (2018) so that a significant portion of assigned rupture would occur on the main megathrust. South of 47°N, this splay fault was originally hypothesized by Priest and others (2010) based on the interpretation of very limited seismic data and some geological reasoning. There was no observational evidence for or against its presence in the north. It is present in slightly different forms in several publications (Priest and others, 2010; Witter and others, 2013; Gao, 2016; Gao and others, 2018; Sypus, 2019) and came to be known by the Cascadia tsunami hazard research community as the "extended L1 model."

Continuing with the names used for hypothetical Cascadia splay faults in Gao and others (2018) and Sypus (2019), we call the other splay fault shown in **Figure 2.4** Splay D. Its southern portion is in the same location as Splay B, but the northern portion of the splay trace is interpreted to merge with the deformation front, around 47°N. The decision for this merging was based on the analysis of CASIE21 data and USGS sparker imaging by the CASIE21 team and the CSWG. This analysis found no evidence for the presence of a splay fault farther north and found limited evidence to hypothesize a potential splay fault to the south. The geometry was adjusted using interpreted picks from a few CASIE21 profiles (PD08, PD09, and PD10; personal communications, Tobin, Ledeczi, and Lucas, 2023). Other structural details of the accretionary prism from these and other CASIE21 profiles are summarized in Ledeczi and others (2024). Utilizing these picks, it was determined that the limited evidence from profiles PD09 and PD10 suggests a dip angle near 45°, whereas profile PD08 suggests a slightly shallower dip. Accordingly, we assigned a generalized 45° dip for both Splay D and Splay B.

2.3 Frontal Thrust and Trench-Breaching Rupture

The trench-breaching rupture involves a frontal thrust (**Figure 1.1**) yet observed seaward-vergent thrusts in the frontal area of the accretionary prism are of limited strike length. It is geologically implausible to have a single frontal thrust activated in one earthquake over a long-distance along strike. As argued by Gao and others (2018) and Wang and others (2024), the use of a hypothetically long single frontal thrust is a worst-case representation of the collective effect of numerous secondary faults in the frontal area to accommodate trench-breaching slip in the presence of thick trench sediment.

With the help of the CSWG and the CASIE21 team, we summarized the presence of seaward- or landward-vergent frontal thrusts near the deformation front (**Figure 2.5**, personal communications, Goldfinger; Watt; Han, 2023). Where there is evidence for seaward-vergent thrusts, including areas with a mixture of seaward and landward vergence, we assume that trench-breaching rupture is possible. Off of the Washington coast, there is almost no evidence for seaward-vergent frontal thrusts (**Figure 2.5b**). Here we assume that large slip of the shallow part of the megathrust does not break the seafloor by activating a frontal thrust but instead, causes widespread, diffuse plastic deformation of the frontal region of the

overlying accretionary prism as argued by Ma (2012) and Wilson and Ma (2021). As discussed by Wang and others (2024), it is reasonable and convenient to use an elastic model to simulate this assumed plastic deformation. Thus, the resultant model is a version of buried rupture, but with a highly updip-skewed slip distribution (see **Sections 3.4** and **5.3**). Therefore, the trench-breaching scenarios produced in this study include this segment of buried rupture. In subsequent descriptions of trench-breaching scenarios (Section **5.3**), we generally do not further explain this anomalous segment unless necessary.

The dips of frontal thrusts, predominantly informed by the CASIE21 profiles, exhibit a general range from 30° to 50° across the Cascadia margin. Our construction of the hypothetical single frontal thrust accounts for such along-strike variations. The Mendocino triple junction (MTJ) region features a notably steep thrust (50° to 60°).

Figure 2.4. Traces of the two assumed splay faults used for modelling. Splay B (or "extended L1") is shown in blue and the new Splay D trace is in green. South of 46.5°N, the two traces fully overlap. Yellow squares are the interpreted splay-fault locations from the CASIE21 profiles.

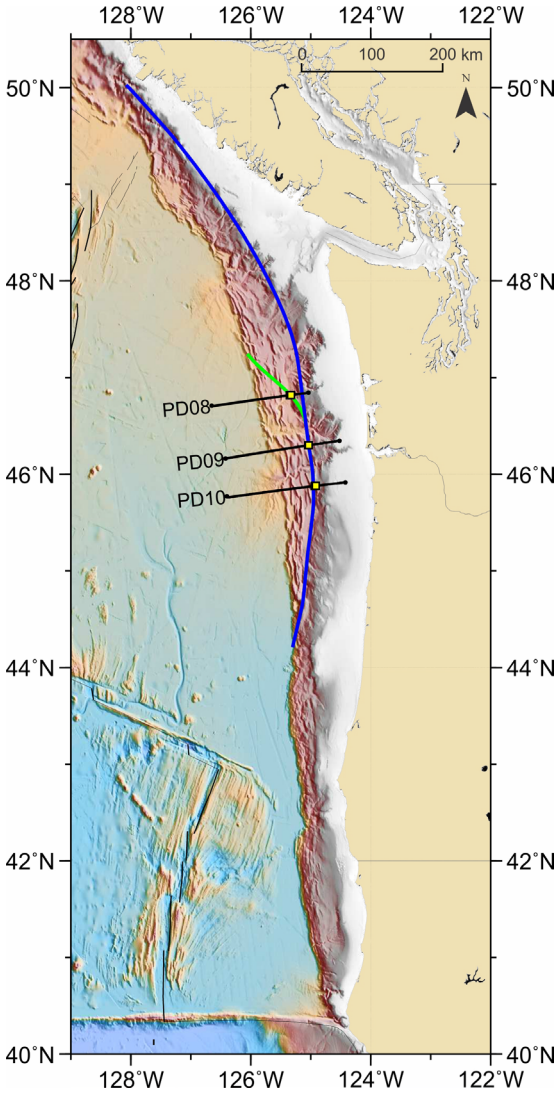

Figure 2.5. Information regarding the frontal thrust geometry. The top left illustration shows hypothetical seaward and landward vergence faulting in cross section view. A) Vergence directions in the frontal accretionary prism compiled by CSWG members Janet Watt and Chris Goldfinger. B) Vergence directions compiled by CASIE21 member Shuoshuo Han. C) Simplification for modeling trench-breaching rupture scenarios. Where there is any evidence for seaward-vergent thrust faulting (yellow), a single frontal thrust is used. Where there is no such evidence (green), highly up-skewed buried slip is assumed.

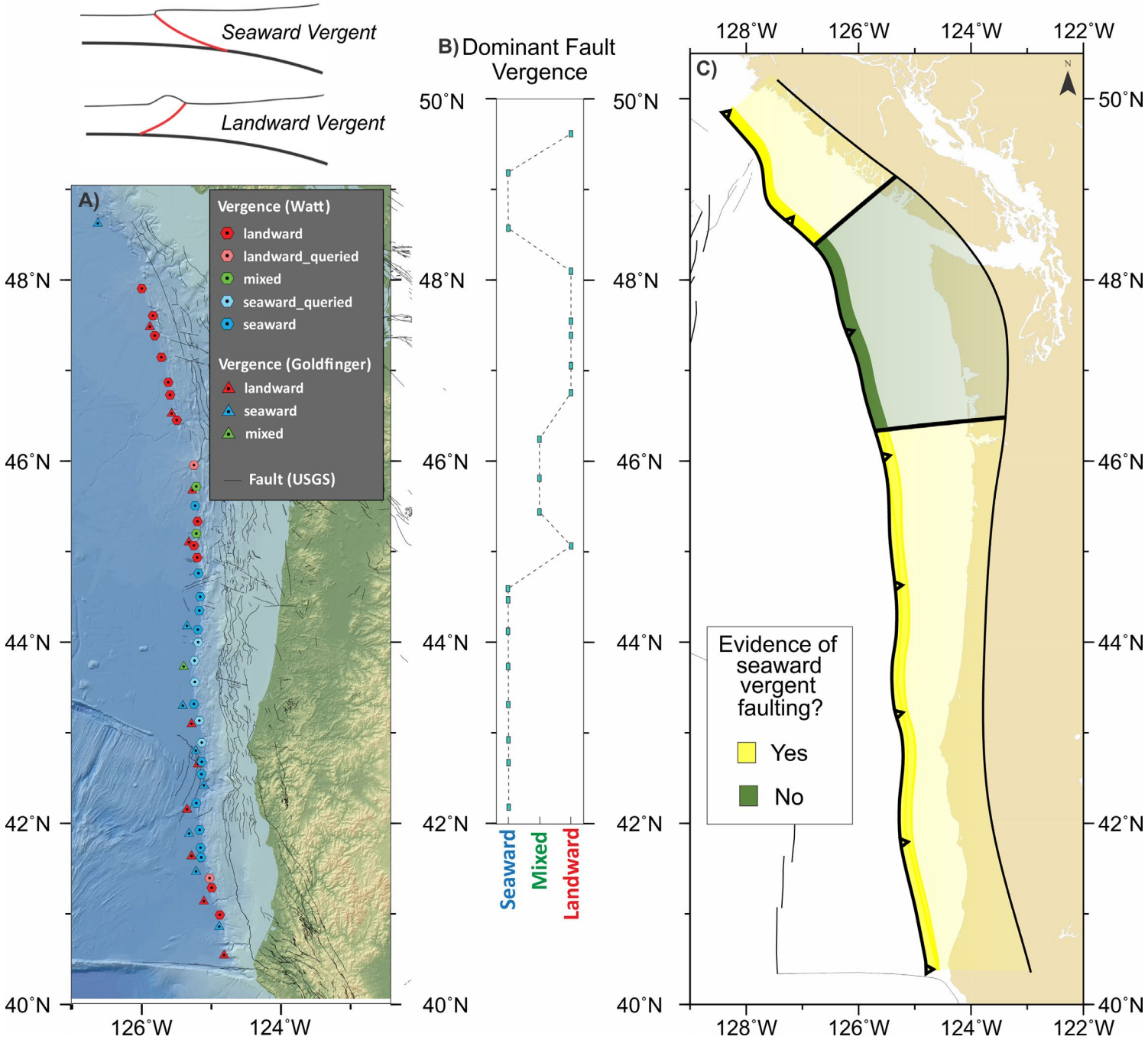

3.0 MODELLING METHOD

3.1 3D Dislocation Model

We used the computer code *Disl3d14*, developed by co-author Wang, to calculate the coseismic seafloor uplift for the suite of rupture scenarios; additional information about Disl3d14 may be found in Gao and others (2018). *Disl3d14* integrates point-source dislocation solutions (Okada, 1992), known as Green's functions, over a fault with realistic 3-D geometry in a uniform elastic half-space. It yields displacement, strain, and stress change at selected observation points, either on the surface of the half-space, along the fault itself, or elsewhere within the half-space. In terms of fault mesh construction and slip vector assignments, this code is fundamentally different from the simpler dislocation codes used by Flück and others (1999) and Wang and others (2003). *Disl3d14* has been used extensively in previous megathrust earthquake modeling at Cascadia (e.g., Priest and others, 2010; Witter and others, 2011; Wang and others, 2013; Gao and others, 2018; Sypus and others, 2019) and other subduction zones (e.g., Brown and others, 2015).

In modeling rupture with Disl3d14, a mesh of triangular elements is used to describe the 3D fault surfaces described in Section 2.0, including an adjustment to the geometry of the shallow part to be described in Section 3.2. For a uniform elastic half space, there is only one independent elastic modulus (Okada, 1992). As in previous Cascadia studies, we fix the Poisson's ratio at 0.25. No other parameters are needed. For prescribed fault slip, ignoring the heterogeneity of the rigidity distribution in real subduction zones, especially the lower rigidity of the frontal accretionary prism, causes little error in predicted tsunamigenic deformation (Carvajal and others, 2022; Wang and others, 2024).

3.2 Effects of Sloping Seafloor in a Flat-Surface Model

The Green's functions from Okada (1992) are precise mathematical solutions for shear dislocation in a uniform elastic half space with a flat upper surface. However, the actual subduction zone has an irregular seafloor slope/shape. Following previous Cascadia modelling studies such as Wang and others (2003), Priest and others (2010), Witter and others (2011), Gao and others (2018), and Sypus (2019), we make an adjustment to the dip of the shallow part of the megathrust so that the fault depth in the flat-surface model is similar to the real fault depth below the seafloor (**Figure 3.1**). This adjustment is particularly crucial for trench-breaching scenarios but less important for deeply buried ruptures.

The adjustment modifies the fault dip to approximately the sum of the seafloor slope angle (α) and the actual near-trench fault dip (β). The resultant greater fault dip causes more vertical seafloor deformation near the trench. In the flat-surface model, this enhanced vertical deformation compensates for the absence of the seaward motion of movement on a sloping seafloor, as illustrated in **Figure 3.1b**. An assessment for this compensation is provided by Wang and others (2018). Without this adjustment, the seafloor rise (u) due purely to the seaward motion of the sloping seafloor is $u = s\sin(\alpha+\beta)/\cos\alpha$, with s representing the fault slip (**Figure 3.1**). After the adjustment, the seafloor rise is $u' \approx s\sin(\alpha+\beta)$. Given that α is typically a small angle, so that $\cos\alpha \approx 1$, we have $u \approx u'$.

This adjustment yields very accurate results for both trench-breaching and buried rupture scenarios, as shown by the examples in **Figure 3.2**. In these examples, the more realistic model with a sloping seafloor is derived using the finite element method. For the finite element model (red), the tsunamigenic seafloor deformation shown in the top panel is a combination of vertical deformation and the uplift due to seaward motion of the sloping seafloor. For the dislocation model (black) with a flat top, but with the

fault dip adjustment explained above and in **Figure 3.1**, the tsunamigenic seafloor deformation is only the vertical deformation, the same as shown in the middle panel. **Figure 3.2** shows, even for the purposely exaggerated very large seafloor slope considered here, the dislocation model with fault adjustment agrees with the finite element model extremely well. This adjustment only addresses the long-wavelength topography missing in the flat-surface dislocation model. Additional short-wavelength effects on tsunami generation can be addressed by applying the gradient correction method of Tanioka and Satake (1996).

Figure 3.1. Adjustments to fault geometry in models with a flat top (from Sypus, 2019). These illustrations show before (solid red line) and after (solid blue line) adjustments to the megathrust fault and seafloor. A) Adjustment for subduction zones with little or no sediment covering the trench. Dashed box indicates the area shown in B). B) Schematic illustration of how the missing effect of the seaward translation of the slope seafloor in a flat surface model can be compensated for with the added uplift enabled by the fault dip adjustment. C) Fault adjustment for subduction zones with thick sediment. The megathrust is still buried at the trench after the adjustment, but a frontal thrust (green dashed line) enables trench-breaching rupture.

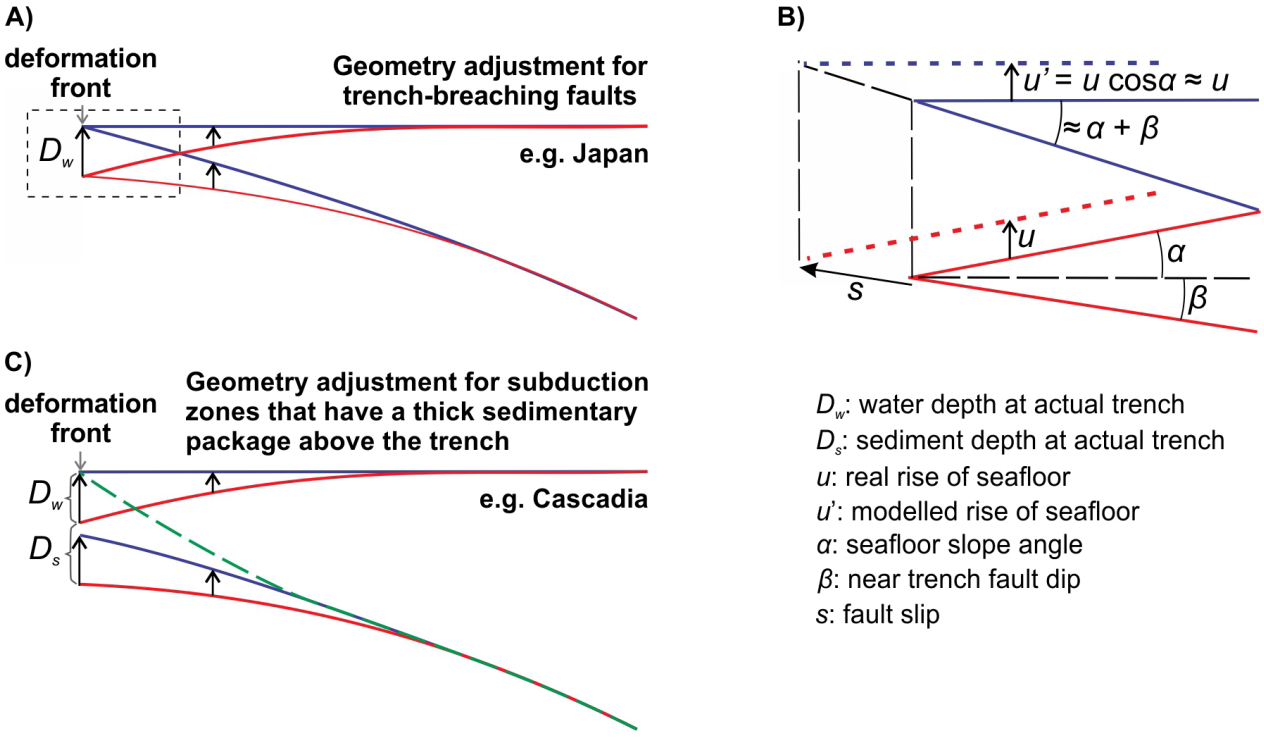

Figure 3.2. Trench-breaching (left) and buried (right) rupture examples to show the effectiveness of the fault dip adjustment shown in Figure 3.1, with uniform rigidity (any value) and Poisson's ratio (0.25). A) Results for the reality model incorporating topography (red) are obtained using the finite element method (Carvajal and others, 2022), and those for the flat-surface model (black) by integrating the point-source dislocation solution of Okada (1985). B) Tsunamigenic seafloor uplift from both models. C) For the flat surface model, the uplift is simply the vertical displacement. For the reality model, the total uplift is the vertical displacement plus the uplift due to the horizontal motion of the sloping seafloor. The step in the total uplift at 50 km from the trench is associated with the topographic kink in the model geometry.

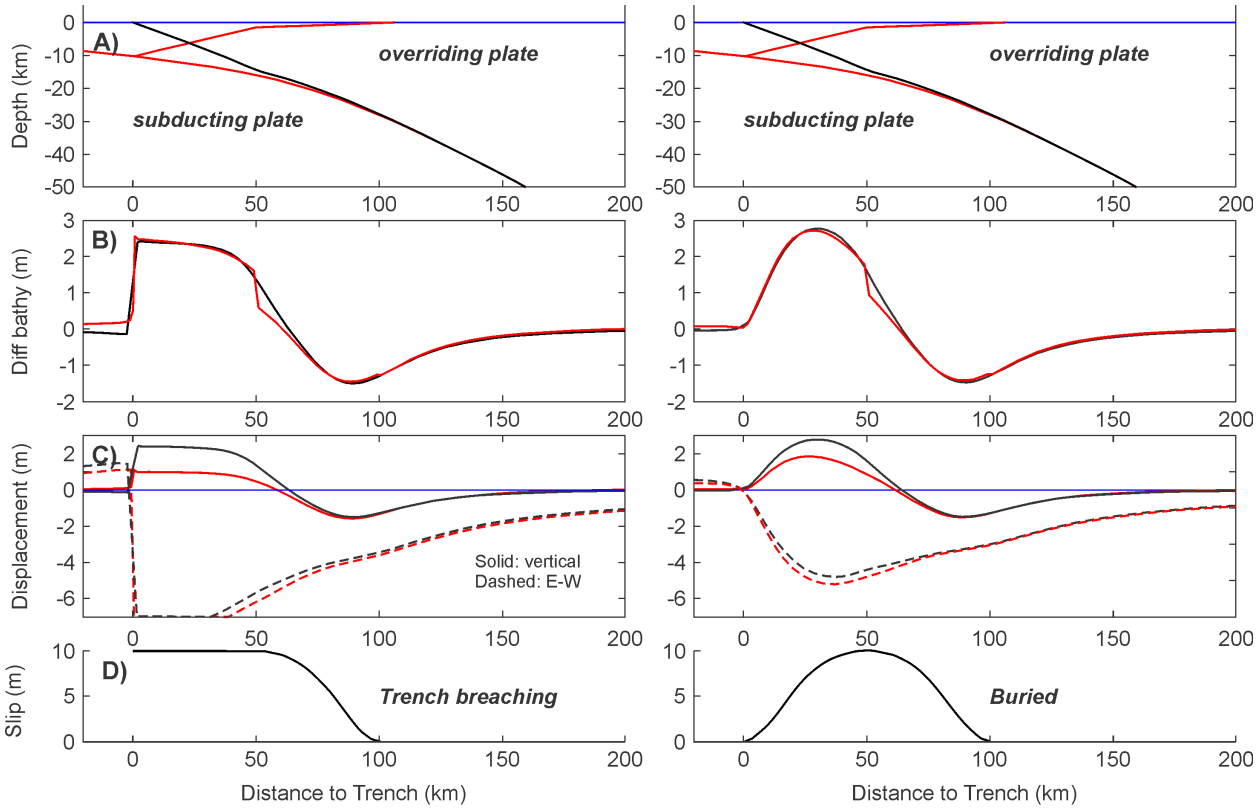

If the fault adjustment was made by simply subtracting the actual bathymetry from the fault geometry described in Section 2.0, it would introduce unrealistic geometry for the adjusted fault used for the modeling. In this study, we first smoothed the actual bathymetry (**Figure 3.3a**) with a low-pass Gaussian filter using a 60-minute standard deviation (**Figure 3.3b**) and then subtracted the smoothed version from the original fault geometry (**Figure 3.3c**) to obtain the adjusted geometry (**Figure 3.3d**). In comparison to **Figure 2.2**, **Figure 3. 4** shows the adjustments made to the initial geometry from Section 2.1. Careful placement of zero-depth control points and the incorporation of additional control points ensure the functionality of the splay and trench-breach geometries. Note that the fault at the deformation front still remains buried beneath the 2 km–4 km sediment after the dip adjustment. Trench-breaching ruptures for Cascadia are modeled by activating a frontal thrust, as explained in Section 2.3. **Figure 3. 4** shows the frontal thrust and splay faults used in our modeling.

Figure 3.3. Bathymetry and fault dip adjustment. A) Actual bathymetry (from GeoMapApp; Ryan and others, 2009). B) Filtered smooth bathymetry used for the fault geometry adjustment in this study. C) Fault geometry before the adjustment (same as in Figure 2.1c). D) Fault geometry after the adjustment.

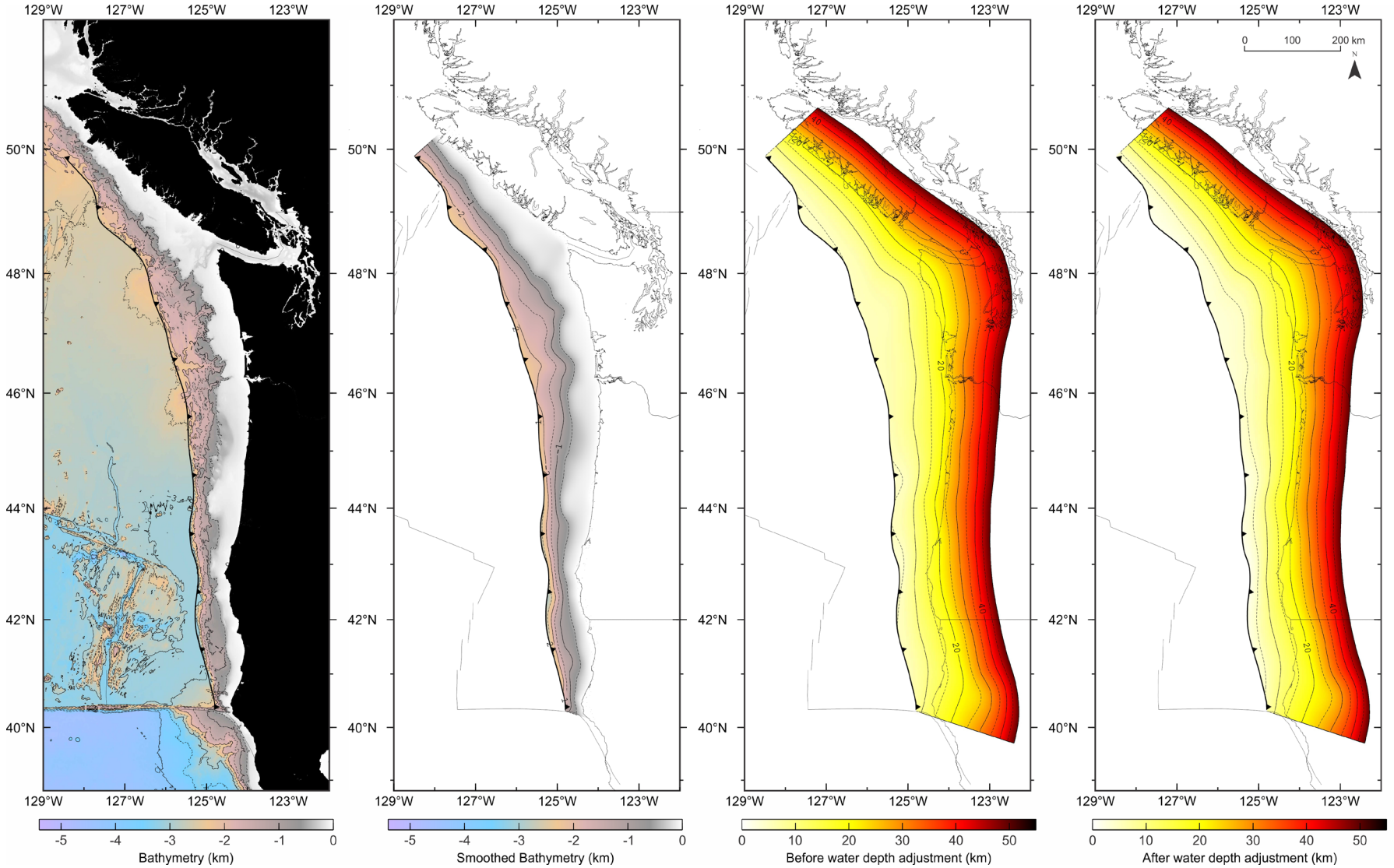

Figure 3.4. Profiles showing how the new geometry, water-adjusted geometry, trench-breaching geometry, and splay-faulting geometries and bathymetry relate. Blue and orange dots are interpreted as depth of the TOC and shallower sedimentary décollement (Carbotte and others, 2024). Darker blue and brown dots are projected interpreted depths from crossing profiles. Red triangle: Deformation front (DF) used in disl3d models. Brown triangle: Coastline.

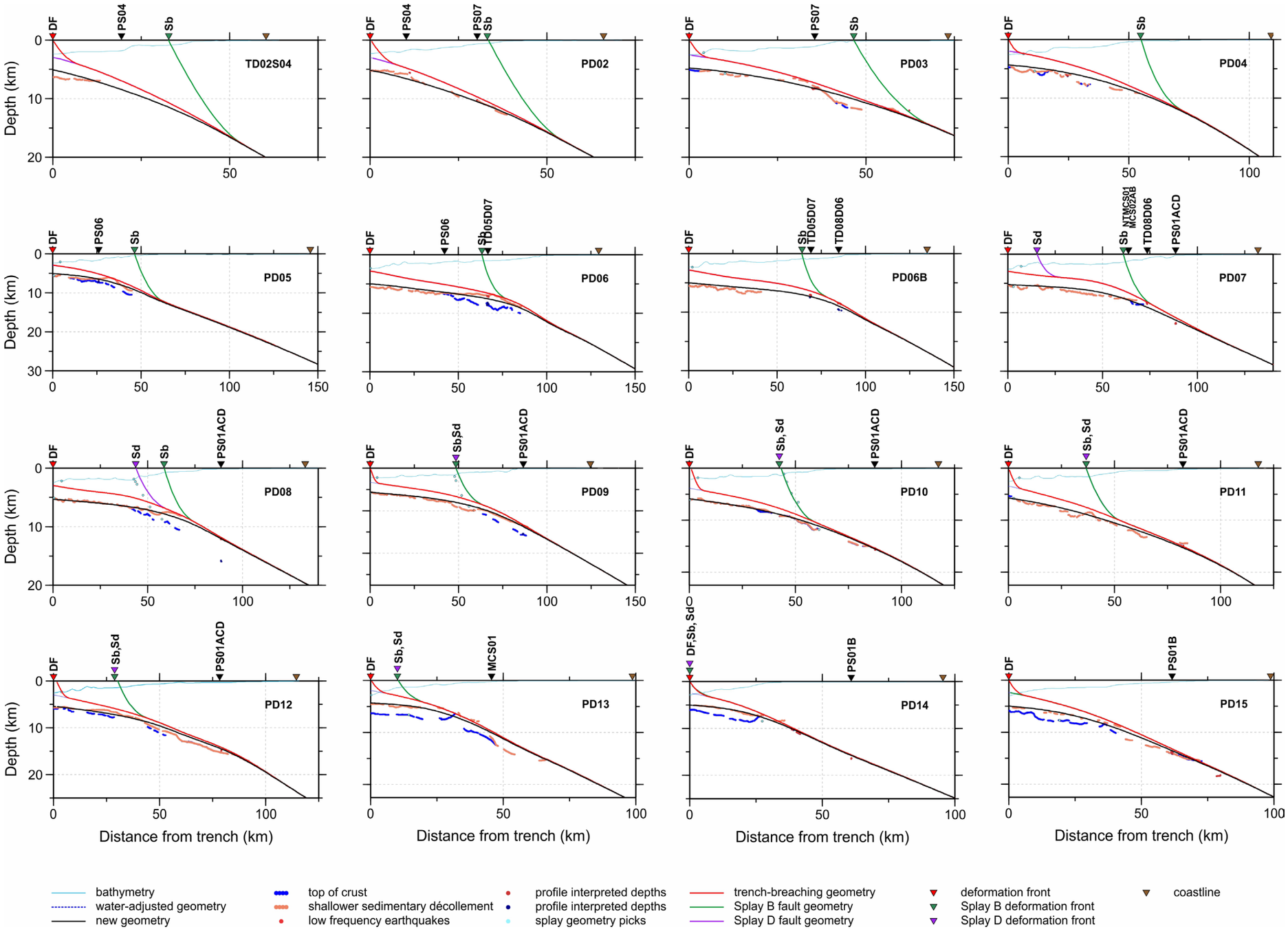

Figure 3.4 (cont.). Profiles showing how the new geometry, water-adjusted geometry, trench-breaching geometry, and splay-faulting geometries and bathymetry relate. Blue and orange dots are interpreted as depth of the TOC and shallower sedimentary décollement (Carbotte and others, 2024). Darker blue and brown dots are projected interpreted depths from crossing profiles. Red triangle: Deformation front (DF) used in disl3d models. Brown triangle: Coastline.

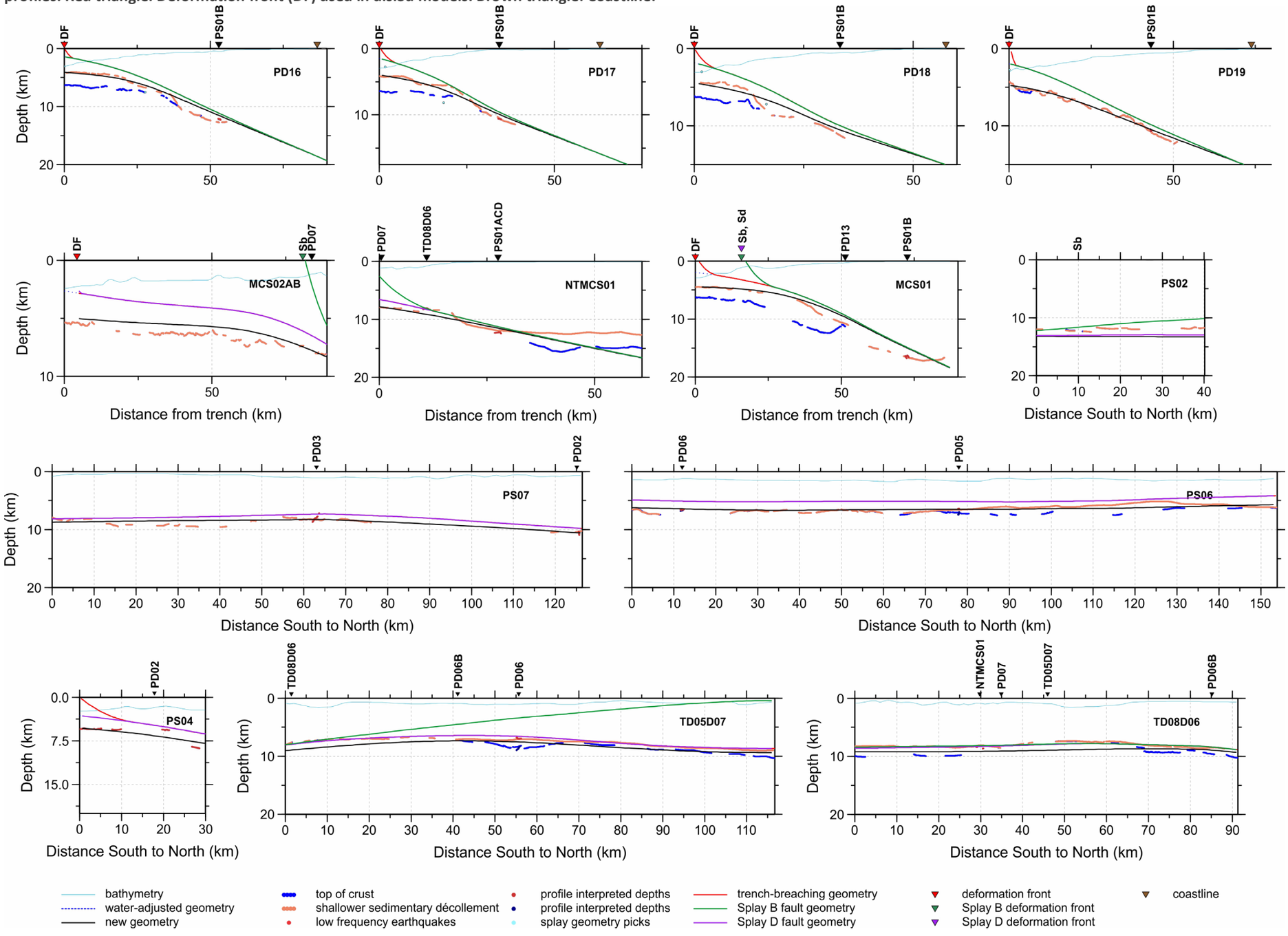

Figure 3.4 (cont.). Profiles showing how the new geometry, water-adjusted geometry, trench-breaching geometry, and splay-faulting geometries and bathymetry relate. Blue and orange dots are interpreted as depth of the TOC and shallower sedimentary décollement (Carbotte and others, 2024). Darker blue and brown dots are projected interpreted depths from crossing profiles. Red triangle: Deformation front (DF) used in disl3d models. Brown triangle: Coastline.

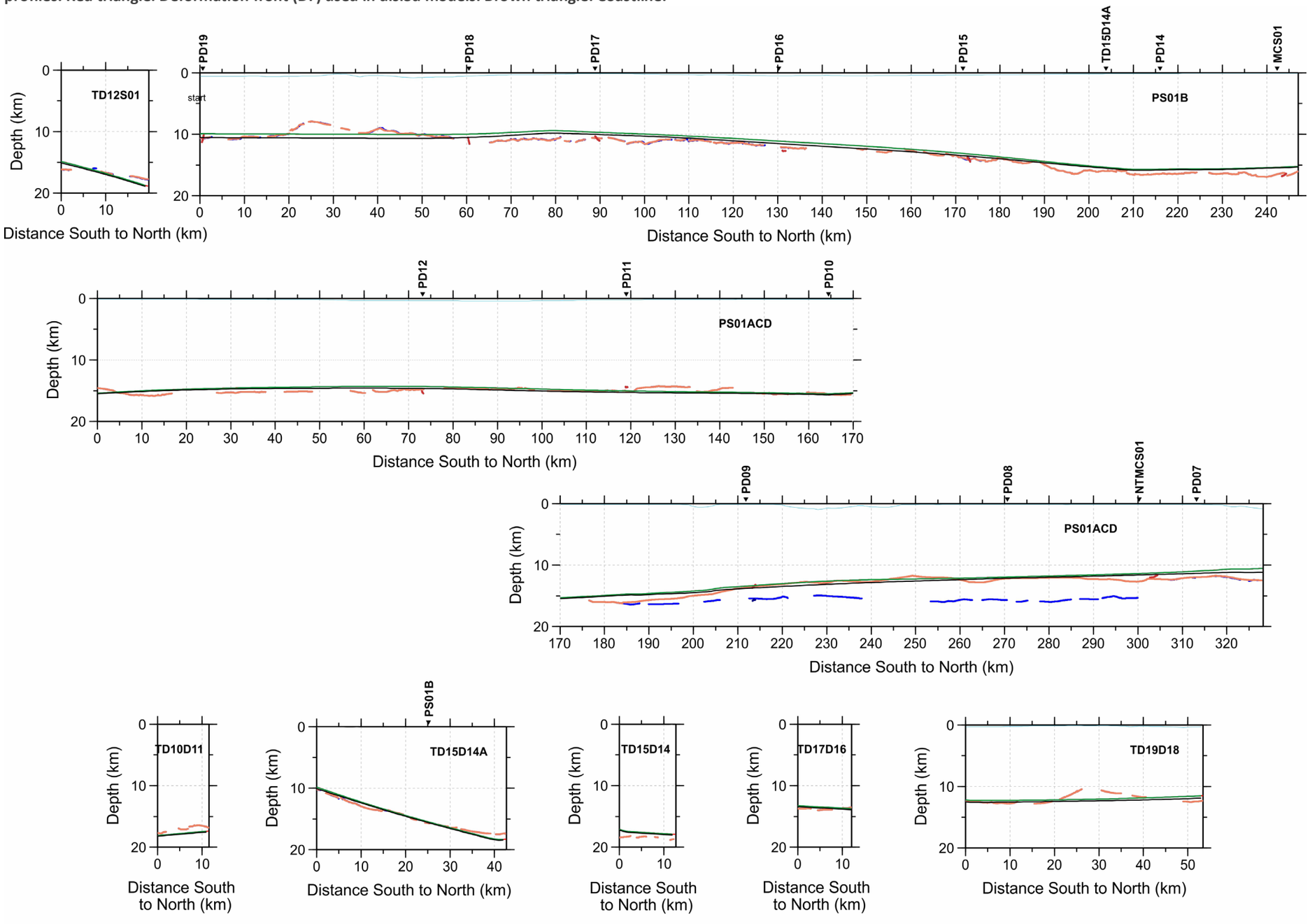

3.3 Constructing 3D Fault Mesh

The fault mesh comprises numerous planar triangular elements to enable numerical integration of the Green's functions along the curved fault. Unlike the schematic illustration in **Figure 3. 5**, triangle size in the fault mesh can vary smoothly over a large range. Each triangle is an integration element and hosts a point-source slip vector at its centroid. The potency of the point source multiplied by the area of the triangle is the average slip of the triangular fault patch. A point where deformation and/or stress is calculated, called the "observation point," must be located away from the fault. This offset distance must be several times the dimension of the fault mesh triangles, so that these discrete point-source triangles can adequately represent a continuous slip distribution. For example, if deformation is to be derived near fault traces (where the fault breaks the seafloor), very small mesh triangles must be used. For trench-breaching and splay-faulting scenarios in this study, we may calculate deformation as close as 150 m to the fault trace on the foot-wall side and 1.0 km on the hanging-wall side. Therefore, the triangles adjacent to the fault trace are only of approximately 300 m linear dimension. However, it would be a waste of computer time to use tiny triangles also for the deeper part of the fault. Therefore, we let the triangle size increase with depth up to about 8 km in the deeper part of the fault. When using the deformation results as input for wave modeling, tsunami modelers can maintain or downgrade the spatial resolution of these results in accordance with their scientific objectives.

To create the fault mesh, we first create a rectangular-shaped mesh in a horizontal plane and then map this regular mesh to the actual fault to create the curved mesh in 3-D (**Figure 3. 5**). Many operations, especially some of those in assigning slip distributions (**Section 3.4**), are readily performed in the rectangular mesh (2-D Cartesian coordinates) before mapping to the curved mesh (curvilinear coordinates).

Figure 3.5. Construction of fault mesh in the dislocation model. A) A simplified map view of the curved 3-D real fault model (depth dimension not shown). The integration triangles employed in the modeling are notably finer than depicted here. B) The rectangular mesh to be mapped onto the real fault. Note that the slip vectors used for numerical integration are at the centroid of the triangular elements, obtained by averaging the three nodal vectors for each element. The direction of the vectors is assigned in the real fault mesh, but their magnitude and spatial variation are assigned in the rectangular mesh.

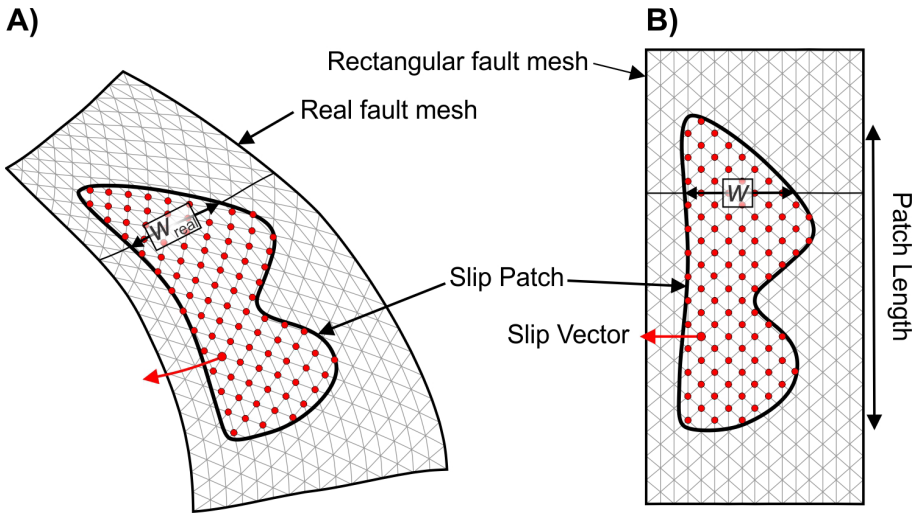

3.4 Assigning Slip Vectors

For any real earthquake, the slip vectors can be directly imported from a published slip model, as was described in Brown and others (2015). However, in deriving predictive tsunami source models, we need to assign the size and rake of the slip vectors. We first calculated slip vectors using relative plate motion Euler vectors and then modify the spatial variations of the magnitude using empirical scaling functions with very few parameters, which will be described below. The Euler vectors for Cascadia, which approximately account for secular block motions of the upper plate, are described in Wang and others (2003). Typically, the value of peak slip in a scenario earthquake is calculated based on the accumulated slip deficit over time, which is the result of multiplying the equivalent duration of the deficit accumulation by the rate of local plate convergence. The spatial decrease of the slip values from the peak value is controlled by the empirical functions.

Using the mapping concept illustrated in **Figure 3. 5**, we can scale the slip magnitude in the strike and dip directions by applying different empirical functions in the Cartesian system of the rectangular fault mesh. In the dip direction, we used the 1-D slip function proposed by Wang and He (2008) based on the original work of Freund and Barnett (1976), with typographic errors corrected in Wang and others (2013):

$$s(x') = s_o\delta\{1 + \sin[\pi\delta^b]\} \tag{1}$$

$$\delta(x') = \begin{cases} \dfrac{6}{q^3}x'^2\left(\dfrac{q}{2} - \dfrac{x'}{3}\right) & 0 \le x' \le \mathrm{q} \\ \dfrac{6}{(1-q)^3}(1-x')^2\left(\dfrac{1-q}{2} - \dfrac{1-x'}{3}\right) & q \le x' \le 1 \end{cases} \tag{2}$$

where s_o is the maximum slip along the profile, $x' = x/w$ represents the downdip distance x, normalized by the local downdip width w, from the top boundary of the rupture zone (**Figure 3.5**). The skewness parameter q varies from 0 to 1, while the broadness parameter b ranges from 0 to 0.3. For buried rupture in this study (**Figure 3.6a**), we use b = 0.2, which produces a distribution similar to that of a typical real earthquake, and let q vary between 0.3, 0.5, and 0.7 to produce updip-skew, symmetric, and downdip-skew slip distributions, respectively. For splay-faulting rupture (**Figure 3.6b**), we simply project the slip vectors from buried rupture scenarios onto the splay geometry. The slip seaward of the splay-fault trace is truncated off, resulting in a smaller seismic moment.

For trench-breaching scenarios the downdip portion of the rupture ($x' \ge q$) is the same as the deeper part of a (symmetric or skewed) bell curve. For the updip portion ($x' \le q$), we use the following function

$$s(x') = s_o\left[f + (1-f)\sin\left(\frac{\pi x'}{2q}\right)\right] \qquad 0 \le x' \le q \tag{3}$$

where f is a constant describing the degree of trench breaching as percentage of s_o. Slip at the trench is $s(0) = fs_o$. Examples for f = 50% and 100% are shown in **Figure 3.6c** and **Figure 3.7a**. For Cascadia, these slip distributions are assigned to a fault geometry with a frontal thrust (**Figure 1.1** and **Figure 3. 4**). Fault mechanics justifications for the kinematic slip distribution function (1) and (2) are discussed by Wang and others (2024).

Figure 3.6. Normalized slip in the margin normal direction. A broadness parameter of b= 0.2 reflects the shown models. A) Updip skewed (red), symmetric (black), and downdip skewed (blue) bell-shape slip distributions with q= 0.3, 0.5, and 0.7, respectively. B) For splay-faulting rupture, the bell shape slip profile is cut off at the fault trace. C) For portions of our trench-breaching rupture, the distribution mirrors the bell shape downdip of the peak slip but tapers updip to the trench to a prescribed percentage of the peak slip.

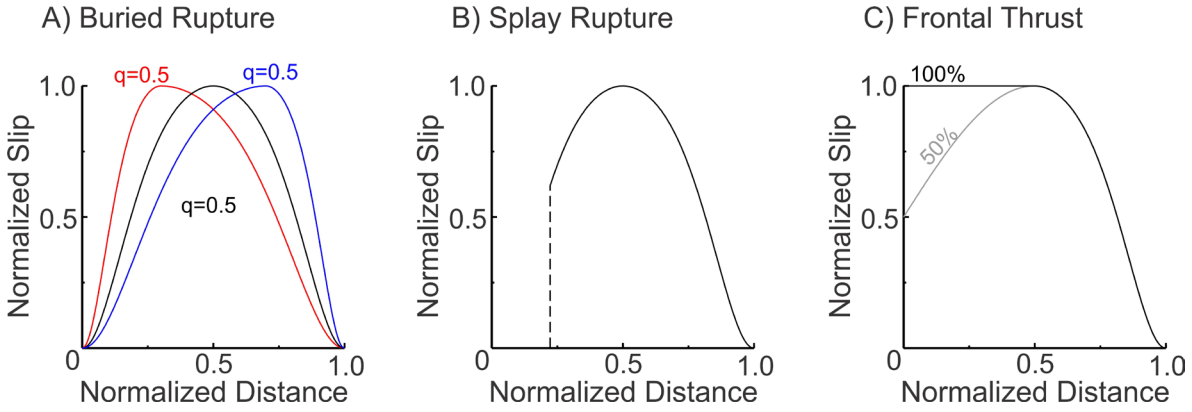

Figure 3.7. Illustration of how the special up-skewed buried rupture (black solid line in (B)) off Washington (green area in Figure 2.5b is constructed by combining the updip part of the q= 0.3 buried slip (black solid in (A)) and the downdip part of the q= 0.5 slip in (B). The slip distributions for the rest of the trench-breaching model where a frontal thrust is involved (yellow areas in Figure 2.5b) are also shown (red and blue) for comparison.

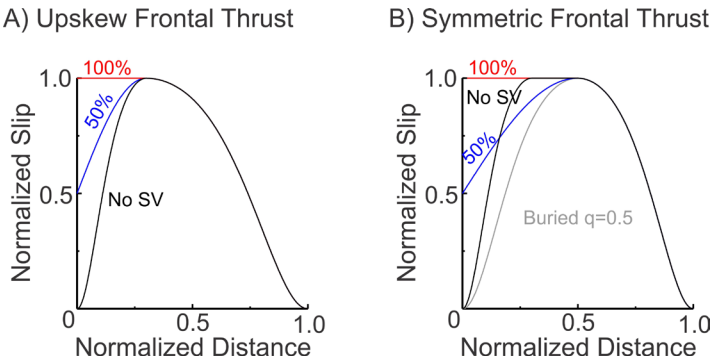

As explained in Section 2.3, our trench-breaching scenarios include an "exception" segment off of the Washington coast (**Figure 2. 5**c) where we use a special type of highly skewed buried rupture (**Figure 3.7**, black curves). The most seaward portion is from the q = 0.3 buried rupture (**Figure 3.7a**), and the most landward portion is from the q = 0.5 buried rupture. They are connected by a section of slip magnitude at the peak value (**Figure 3.7b**).

How the assigned slip magnitude varies along strike depends on specific situations described further in the following section. For imposing segmentation boundaries, such as the two boundaries bracketing the anomalous segment shown in **Figure 2.5b**, we simply use linear tapering over a specified distance. For example, for those in **Figure 2.5b**, the transition distance is 25 km. For depicting along-strike tapering of slip as observed in real earthquakes, we let the magnitude scale with local patch width w as $(w/w_k)^n$, where $k = 1, 2$, and $n \geq 0$ (**Figure 3.8**). Here w_k represents a reference local width at a certain distance from the rupture's ends along the strike direction, and the scaling occurs between this point and the end

of the rupture (**Figure 3. 8b**). The slip magnitude is smaller where $w < w_k$ and becomes zero where $w = 0$ at the termini of the rupture.

Figure 3.8. Schematic illustration of how slip magnitude scales with local rupture zone width w following $(w/w_k)^n$, where $k = 1, 2$. Warmer color indicates larger slip. A) An elliptical rupture patch with $w_1 = w_2 = w_{max}$. B) The more general situation. In this example, slip in the leftmost 30% of the rupture is scaled using w_1, and that in the rightmost 10% using w_2. Figure from Sypus (2019).

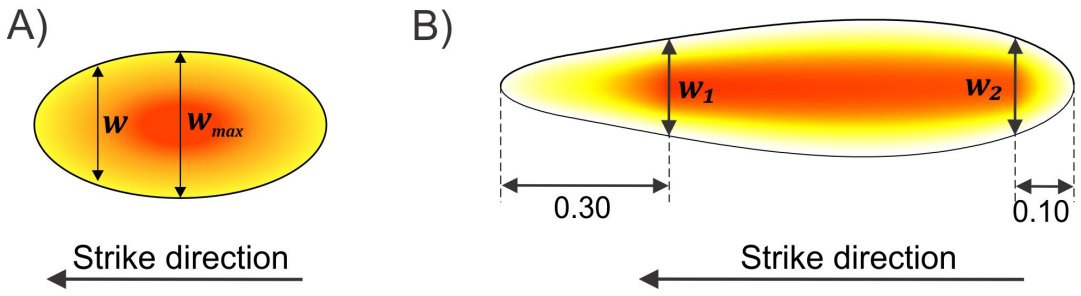

4.0 OVERVIEW OF CASCADIA TSUNAMI SOURCE SCENARIOS

As noted previously, scientists met in Fort Collins, Colorado in 2022 to evaluate the state of knowledge on Cascadia and begin to develop an updated earthquake logic tree for the region that could be used for PTHA (Patton and others, 2022). Since then, work undertaken by the Cascadia deformation model CSWG (this study) has resulted in changes to various parameters and refinements to various branches, resulting in a revised logic tree (**Figure 4.1**). A more detailed description of the steps taken to develop the updated logic tree will be provided in a separate paper being developed by the Powell Center Working Group on Cascadia sources. Hence, this report only describes how the rupture scenarios are constructed, and resultant surface deformation calculated. It does not discuss how the deformation generates tsunami waves and runup and what scenarios are more probable or less probable.

There are two branches to the updated Cascadia logic tree (**Figure 4.1**). The first is referred to as the "USGS" branch, which is based on the updated Western US Seismic Hazard models for Cascadia that use global scaling functions to calculate the earthquake magnitude and rupture characteristics and paleoseismology to constrain earthquake rate models (Peterson and others, 2023). The second branch is referred to as the "DOGAMI" branch, which is modified slightly from the original DOGAMI earthquake logic tree, used previously to simulate tsunami inundation along the Oregon coast (Witter and others, 2011; 2013). The latter branch emphasizes the local geology and paleoseismic studies undertaken in Cascadia to define "T-shirt" size (small, medium, large, extra-large; based on paleoseismic interevent times) full-margin earthquakes that span a spectrum of possible rupture scenarios. Following these two branches are other important aspects controlling the branches of the logic tree (**Figure 4.1**), which include the along-strike rupture length, size of slip deficit, rupture type, shape/depth of rupture, termination depth, and whether we apply a quasi-uniform slip distribution or asperity slip distribution. The logic tree construction was also influenced by operational needs in deriving probabilities. For example, the "Cluster M8" earthquake scenarios partially rupture the margin, but they are attached to the "USGS" part of the "Whole Margin" branch of the logic tree. However, in this report, we still consider them partial ruptures (Section 6.0). A total of 3,502 models were created to meet the needs of this logic tree. The naming convention for these models is shown in **Table 4.1**.

Figure 4.1. Logic tree for a whole margin and partial CSZ rupture constructed by the USGS-NTHMP Cascadia Powell Center Tsunami Sources Working Group and updated by the CSWG. Additional refinements from H.K Thio (*pers. comm., 09-2024*).

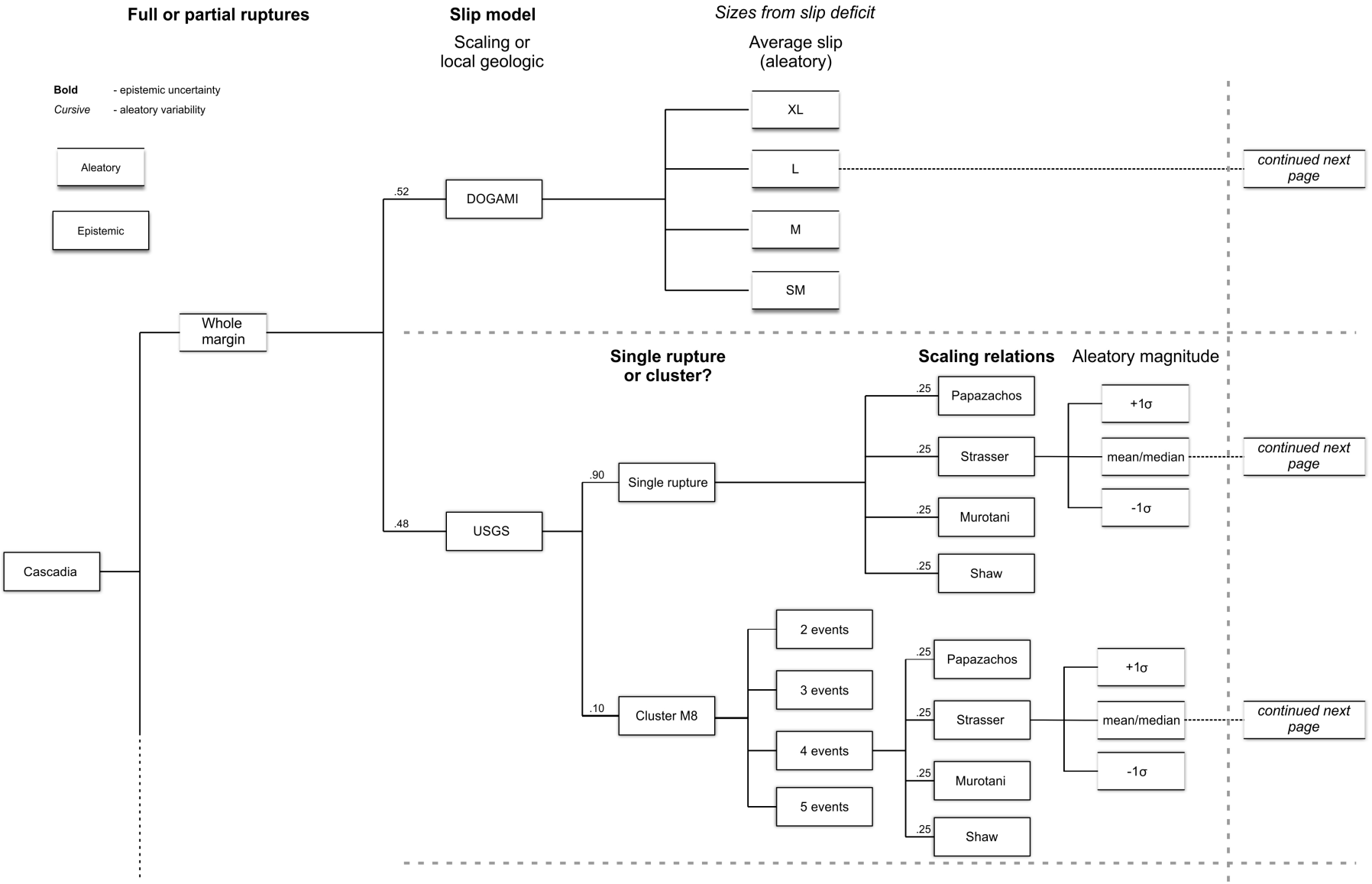

Figure 4.1. (cont.). Logic tree for a whole margin and partial CSZ rupture constructed by the USGS-NTHMP Cascadia Powell Center Tsunami Sources Working Group and updated by the CSWG. Additional refinements from H.K Thio (*pers. comm., 09-2024*).

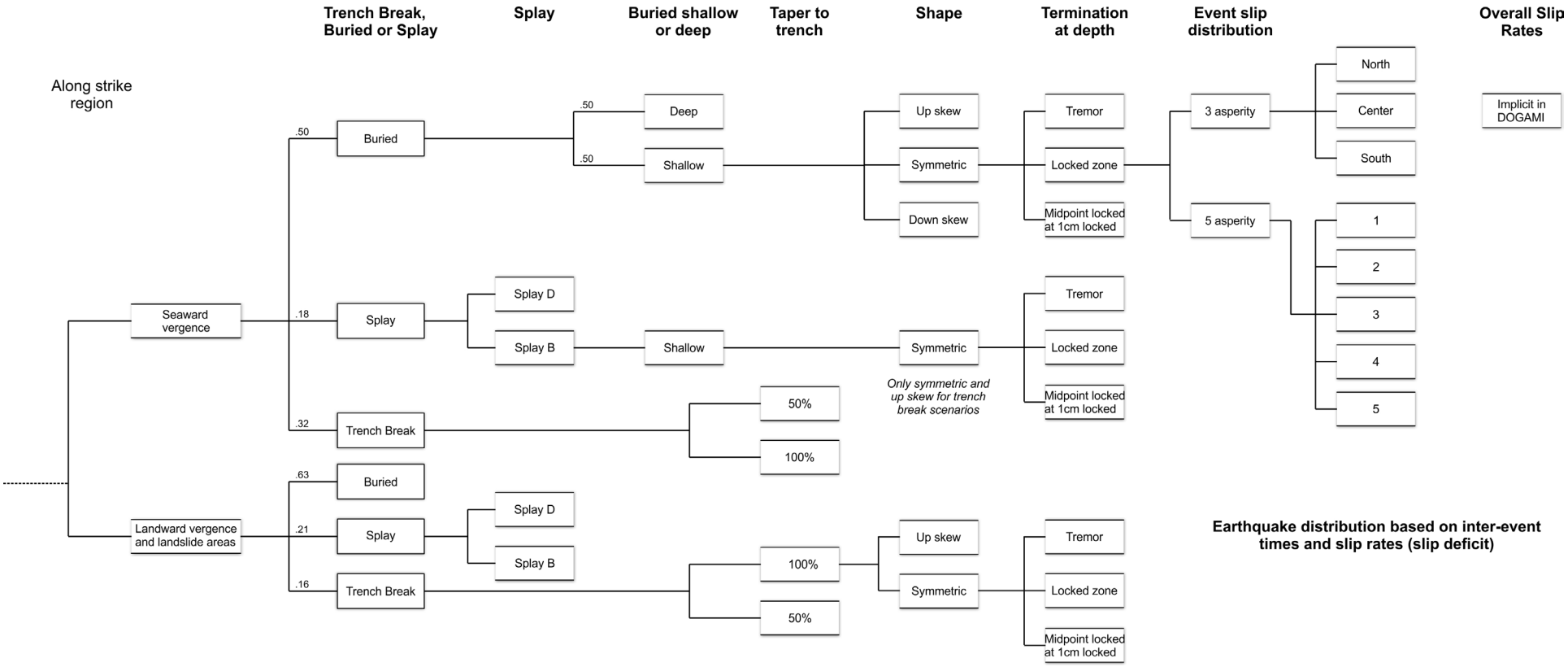

Figure 4.1 (cont.). Logic tree for a whole margin and partial CSZ rupture constructed by the USGS-NTHMP Cascadia Powell Center Tsunami Sources Working Group and updated by the CSWG. Additional refinements from H.K Thio (*pers. comm., 09-2024*).

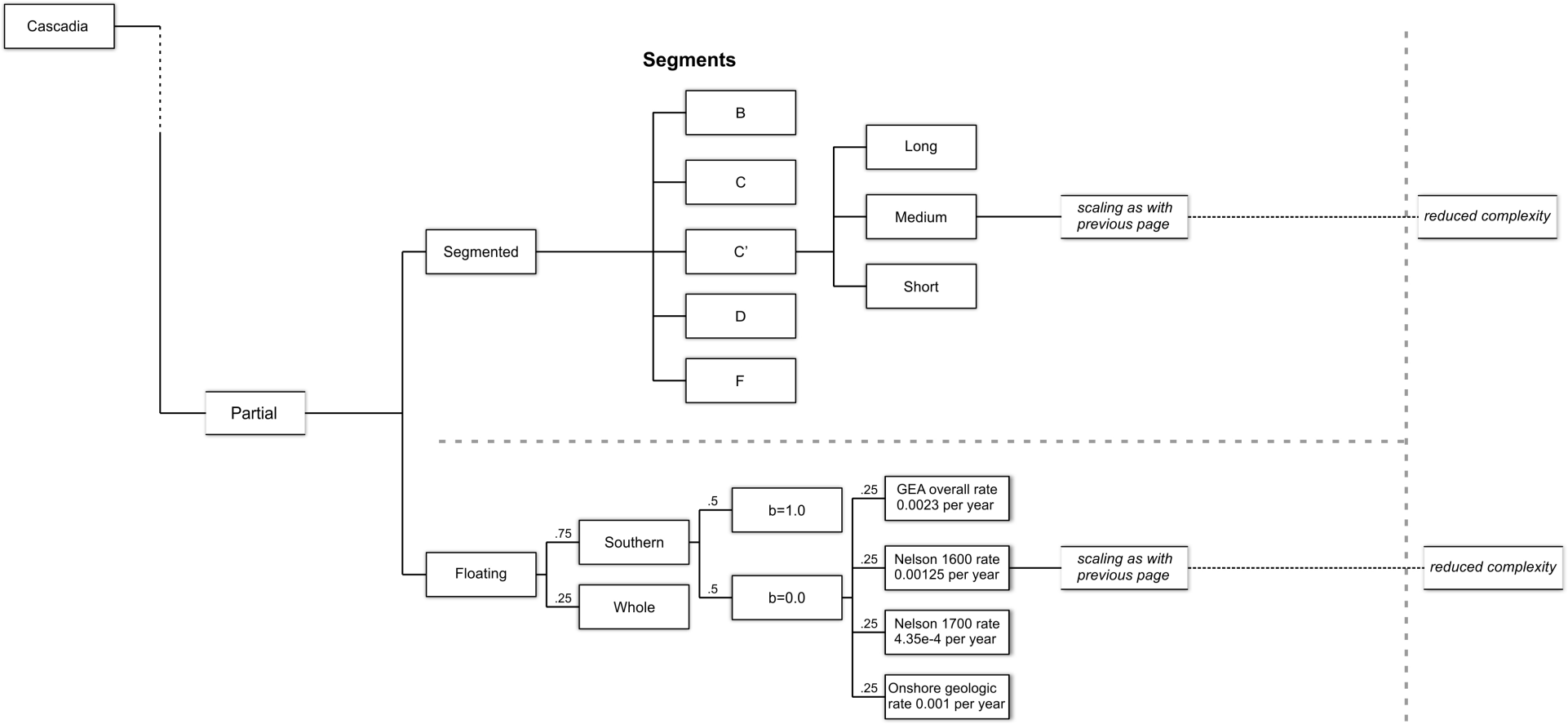

Table 4.1. Naming convention for Cascadia tsunami sources.

Length		**Buried / SplayB / SplayD / Trench Break (50 or 100)**	**Deep / Shallow (only Buried Rupture has Deep Rupture)**	**Shape**	**Termination at depth**	**Event slip distribution**
Aexp / A / Bs / Bm / Bl / Cs / Cm / Cl / Cps / Cpm / Cpl / Ds / Dm / Dl / Fs / Fm / Fl				**Upskew / Symmetric / Downskew**	**Tremor/Locked zone/Midpoint locked and 1 cm locked**	**Uniform slip deficit / Asperity (North, Centre, South)**
Cluster 2-1 / 2-2 / … / 5-5						
Aexp (whole margin with explorer rupture) A (whole margin without explorer rupture) Bs (B short) Bm (B medium) Bl (B long) Cs (C short) Cm (C medium) Cl (C long) Cps (C' short) Cpm (C' medium) Cpl (C' long) Ds (D short) Dm (D medium) Dl (D long) Fs (F short) Fm (F medium) Fl (F long)	See **Figure 4.2**	B (Buried)	D (deep)	UpS	T (Tremor)	U* (Uniform slip deficit)
		Sb (Splay B)	S (shallow)	Sym	L (Locked zone)	AN (Asperity North)
		Sd (Splay D)		DnS	M (Midpoint locked and 1 cm locked)	AC (Asperity Centre)
		T50 (Trench Breaching 50% peak slip to trench)				AS (Asperity South)
		T100 (Trench Breaching 100% peak slip to trench)				A1 (Farthest south of the 5-part asperity models)
						A2
						A3
						A4
CLUSTERS						A5 (Farthest north of the 5-part asperity models)
2-1 2-2 3a-1 … … 5-5	See **Figure 6.1**					
FLOATING						
E1 … … E10	See **Figure 6.3**					

* U3 and U5 are for uniform model of 3-part and 5-part asperity set, respectively.

In the strike dimension, we have four primary rupture categories: whole margin, segmented, clusters, and floating (Prefixes A, Cluster, B–F, and E, respectively, in **Table 4.1**). We will present results for whole-margin ruptures in Section **5.0** and the other three in Section **6.0**. **Figure 4.2** shows the northern and southern limits of the whole-margin (A) and segmented ruptures (B–F). How abrupt or gradual a rupture terminates at the MTJ at the southern terminus of the subduction zone is presently unknown. In this study, we allow a linear north-to-south tapering of slip over a 25-km-wide transition zone centered at 40.492°N. The northern terminus is more complex, involving interactions between the Juan de Fuca (JdF)–Explorer plate (Exp) boundary (Nootka Fault boundary). As described in Section **5.0** we either terminate rupture at this boundary (A) or include the Exp north of it (A+Exp) but with less slip as in Gao and others (2018). We place the boundary 5 km farther north than in Gao and others (2018) in accordance with Hutchinson and others (2019). Similar to the MTJ boundary, a 25-km-wide zone of linear tapering is used here. The other boundaries shown in **Figure 4.2** and those boundaries for the cluster and floating rupture models are discussed in Section **6.0**.

In the dip dimension, we have three types of rupture (**Figure 1.1**): buried, splay faulting, and trench breaching (B, S, and T, respectively, in **Table 4.1**). Boundaries in the dip direction are summarized in **Figure 4.3**. Following Witter and others (2011; 2013), the buried rupture scenarios include the shallow and deep types. In the shallow buried rupture, the bell-shaped megathrust slip tapers to zero at the deformation front (also loosely referred to as the trench in this report). In the deep buried rupture, the bell-shaped slip tapers to zero at a deeper location farther landward off of Washington and northern Oregon (**Figure 4.3**, grey dash line). The possibility of a deep buried rupture was introduced by Witter and others (2011) based on the structural style of the accretionary prism in this area. In Witter and others (2011; 2013), its upper limit extends not as far as the trace of the splay faults and ends more abruptly than shown in **Figure 4.3**. For simplicity and a smoother merging with the deformation front, we let it overlap with the trace of the splay faults (**Figure 4.3**). The splay-faulting scenarios include Splay B and Splay D as discussed in Section 2.2. All the trench-breaching scenarios include an anomalous segment off of Washington (**Figure 2.5b**) where the rupture does not breach the trench but instead is a buried rupture with a highly up-skewed slip distribution (Section 2.3). For all the scenarios, except those in the floating rupture category (Section 6.3), there are three boundaries in the downdip direction based on those used in the National Seismic Hazard Maps (Petersen and others, 2014; Frankel and others, 2015). However, our version of these boundaries is slightly smoother (**Figure 4.3**). For historical reasons, we adopt the names for these three lines given in the caption of **Figure 4.3** and **Table 4.1**, although the specific meaning of these names has evolved or lost scientific significance with time (Wang and Trehu, 2016). From deep to shallow, they are represented by the letters T (tremor), L (locked zone), and M (Midpoint locked and 1 cm locked) in **Table 4.1**. Most of the scenarios include updip-skewed ($q = 0.3$), symmetric ($q = 0.5$), and downdip-skewed ($q = 0.7$) slip distribution (**Figure 3. 6**), called UpS, Sym, and DnS, respectively, in **Table 4.1**.

The peak slip in a model is determined by the assumed period of slip deficit accumulation. A "uniform slip along strike" means a uniform period of slip deficit accumulation. Even without the additional along-strike scaling (**Figure 3.8**), the magnitude of the slip is not uniform because the local convergence rate dictated by the Euler vectors (Section **3.4**) is not uniform along strike. In general, slip is assigned with a 500-year slip deficit. An exception are the "asperity" models to be explained in Section **5.4**. The deformation results from these models can be linearly scaled to any slip deficit. To fulfill logic tree requirements, many of the models will need to be scaled, significantly increasing the total number of scenarios beyond the initial 3,502. These adjustments are crucial for the models to comply with specific criteria, including confining the earthquake magnitude to a specified range in some cases, applying

designated scaling methods like "T-shirt" sizes for segmented scenarios, and adhering to various scaling relations for the USGS branches.

Figure 4.2. Illustration of the two whole-margin (A and A+Exp) models and the along-strike definition of the segmented ruptures. The main segmented boundaries are black while the +/- 50 km boundaries are blue dash.

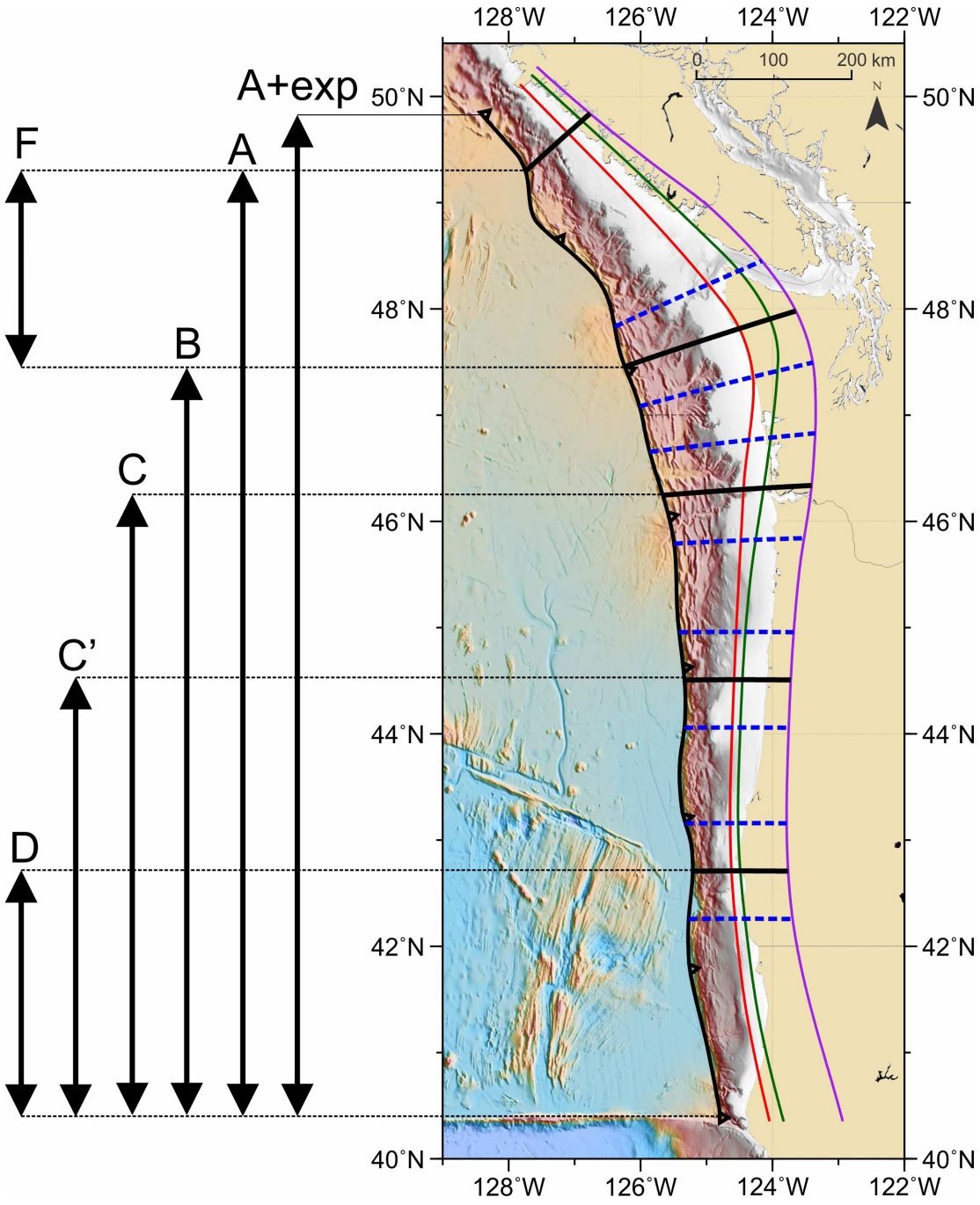

Figure 4.3. Map showing the main dip direction rupture boundaries. The four updip boundaries are the deformation front (black), deep buried rupture termination (grey dash), Splay B (blue), and Splay D (orange). The down-dip boundaries are the midpoint between the fully locked zone and the 1 cm/yr locking contour (M, red), the 1 cm/yr locking contour (L, green), and the top of nonvolcanic tremor zone (T, purple). These three lines are smoothed from those in the USGS seismic hazard model, which are represented by color-coded dots.

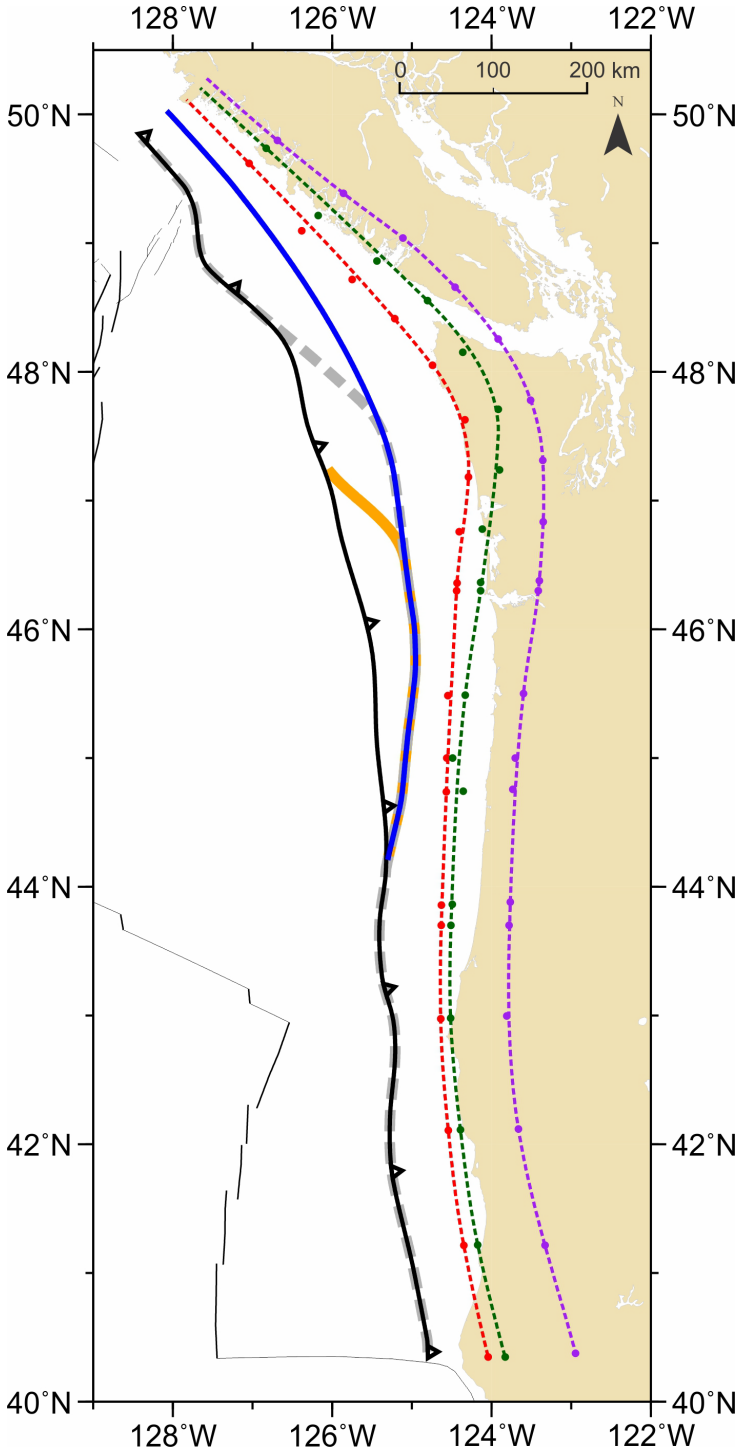

5.0 WHOLE-MARGIN RUPTURE SCENARIOS

Whole-margin rupture scenarios spatially include the rupture areas of segmented and cluster partial rupture scenarios. The whole-margin scenarios thus adequately illustrate the deformation behavior of the different modes of rupture (**Figure 1.1**) and the effects of various rupture boundaries in the dip direction (**Figure 4.3**) also for these partial rupture scenarios. Therefore, most of the figures in this section are also useful for Section **6.0**. Except for the examples designed to illustrate the effect of the three options of the downdip rupture limit (M, L, and T from shallow to deep; **Figure 4.3**), all the examples shown in this section (**Figure 5.1**–**Figure 5.13**) use the intermediate L option.

For the whole-margin ruptures, the southern rupture boundary is at the MTJ (**Figure 4.2**). The northern boundary varies between the USGS and the DOGAMI branches. For the USGS branch, we terminate the northern rupture boundary along a line connecting the Nootka fault with Brook Penisula (A in **Figure 4.2**), to be similar to the USGS NSHM model parameters. For the DOGAMI branch, we allow slip to occur on the Exp with reduced slip (A+Exp in **Figure 4.2**), following Gao and others (2018) and Sypus (2019). Allowing this extra approximately 60 km of fault to slip will result in larger tsunami waves along the coast of northern Vancouver Island, but is unlikely to affect the coast of the United States.

There is an important difference between the whole-margin DOGAMI branch presented here and the original DOGAMI work described by Witter and others (2011; 2013). The original DOGAMI work combines the effect of along-strike variations in recurrence into whole-margin rupture models. Based on the interpretation of offshore turbidite records (Goldfinger and others, 2012; 2017), the Cascadia megathrust ruptures more frequently towards its southern end with smaller slip in each rupture. DOGAMI (whole-margin) source models thus allowed the slip magnitude to decrease in a few steps from north to south, which controlled along-strike variations in tsunami impact on coastal areas. However, the shorter recurrence intervals in the south associated with the smaller slip was accounted for in applying these whole-margin source models to different parts of the Cascadia margin. In accordance with the decision made by the CSWG, the whole-margin source models constructed in the present study does not have the stepwise southward decrease in slip magnitude and thus produces much larger tsunami waves in the southern areas than the models of Witter and others (2011; 2013). The more frequent and smaller tsunami events in the south are separately dealt with in the "Segmented" part of the "Partial" rupture branch of the logic tree, for which the source models are summarized in Section **6.1**.

5.1 Whole-Margin Buried Rupture

The buried rupture models yield smooth distribution of surface deformation, as seen in the examples shown in **Figure 5.1**, **Figure 5.3**, and **Figure 5.5**.

Figure 5.1 compares the shallow and deep buried ruptures in map view and **Figure 5.2** in cross-section view. The updip limit of the deep one is shown using a grey line in **Figure 4.3**. Where it differs from the shallow one, the downdip rupture width is much narrower. With the same peak slip, the narrower rupture results in greater uplift over a narrower area closer to the shore (**Figure 4.3a**) than does the shallow buried rupture. Greater uplift is associated with a greater horizontal shortening of the upper plate due to the sharper updip decrease in fault slip, a greater thickness of the part of the upper plate that is shortened, and a larger dip of the megathrust.

Skewing slip further skews surface deformation (**Figure 5.3** and **Figure 5.4**). Up-skewed slip produces greater uplift closer to the deformation front, but down-skewed slip has the opposite effect and leads to greater coastal subsidence.

Figure 5.1. Examples of the slip of distribution (upper panels) and surface vertical deformation (lower panels) of whole-margin A) deep and B) shallow buried rupture. These two models use symmetric bell slip distribution and the intermediate downdip rupture limit (L). Model scenario names included at top of figure.

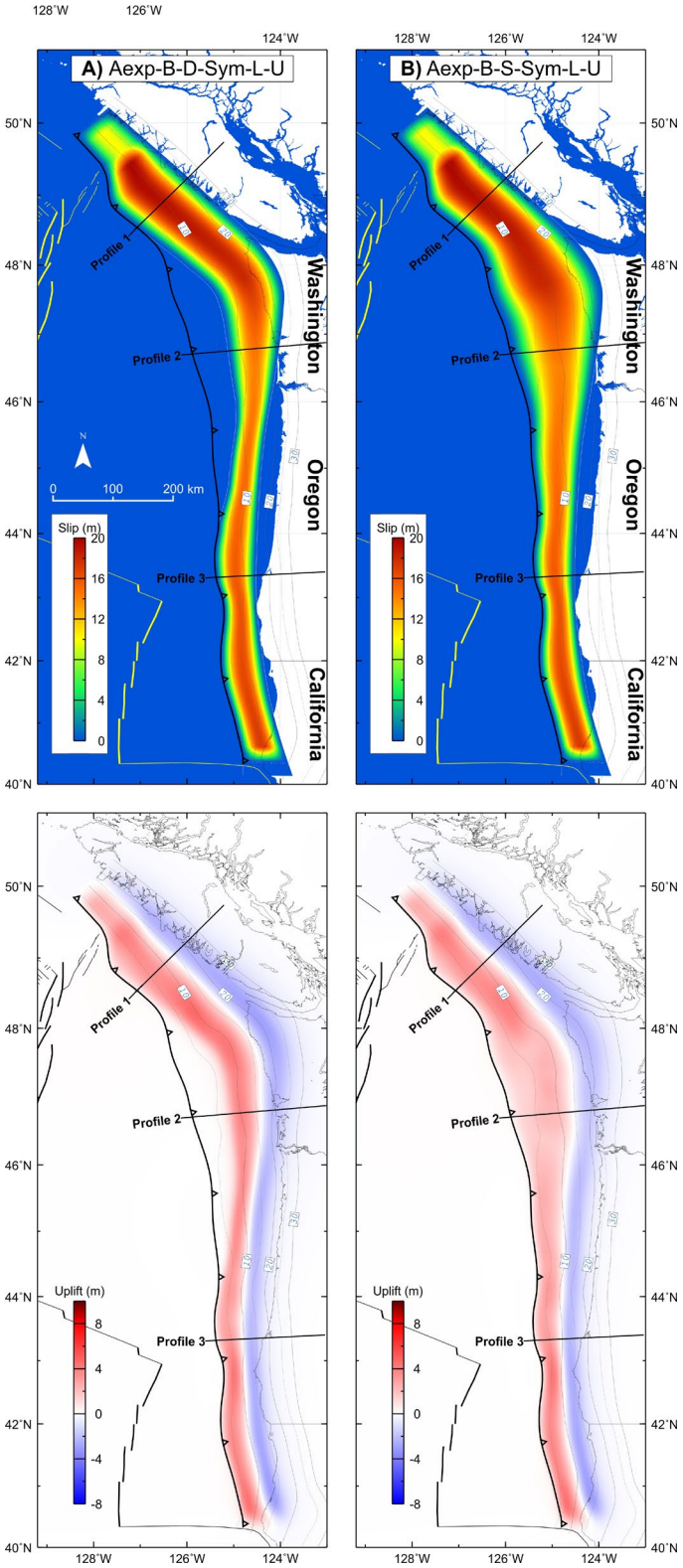

Figure 5.2. Surface deformation, fault slip and fault for profiles 1 to 3 (from north to south) in Figure 5.1, showing results for deep (black lines) and shallow (red lines) whole margin buried rupture scenarios.

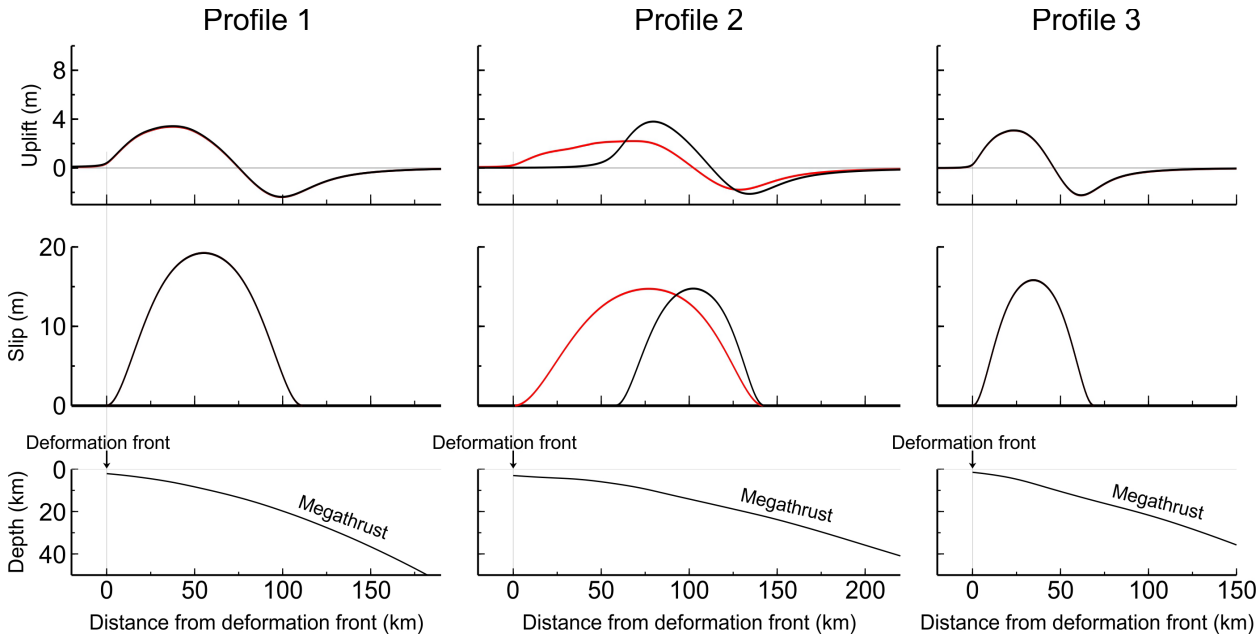

Figure 5.3. Examples of the slip of distribution (upper panel) and vertical deformation (lower panel) of whole-margin (A) up-skew, (B) symmetric, and (C) down-skew buried rupture. These three models use the shallow buried (B-S) rupture and the L downdip limit. Model scenario names included at top of figure.

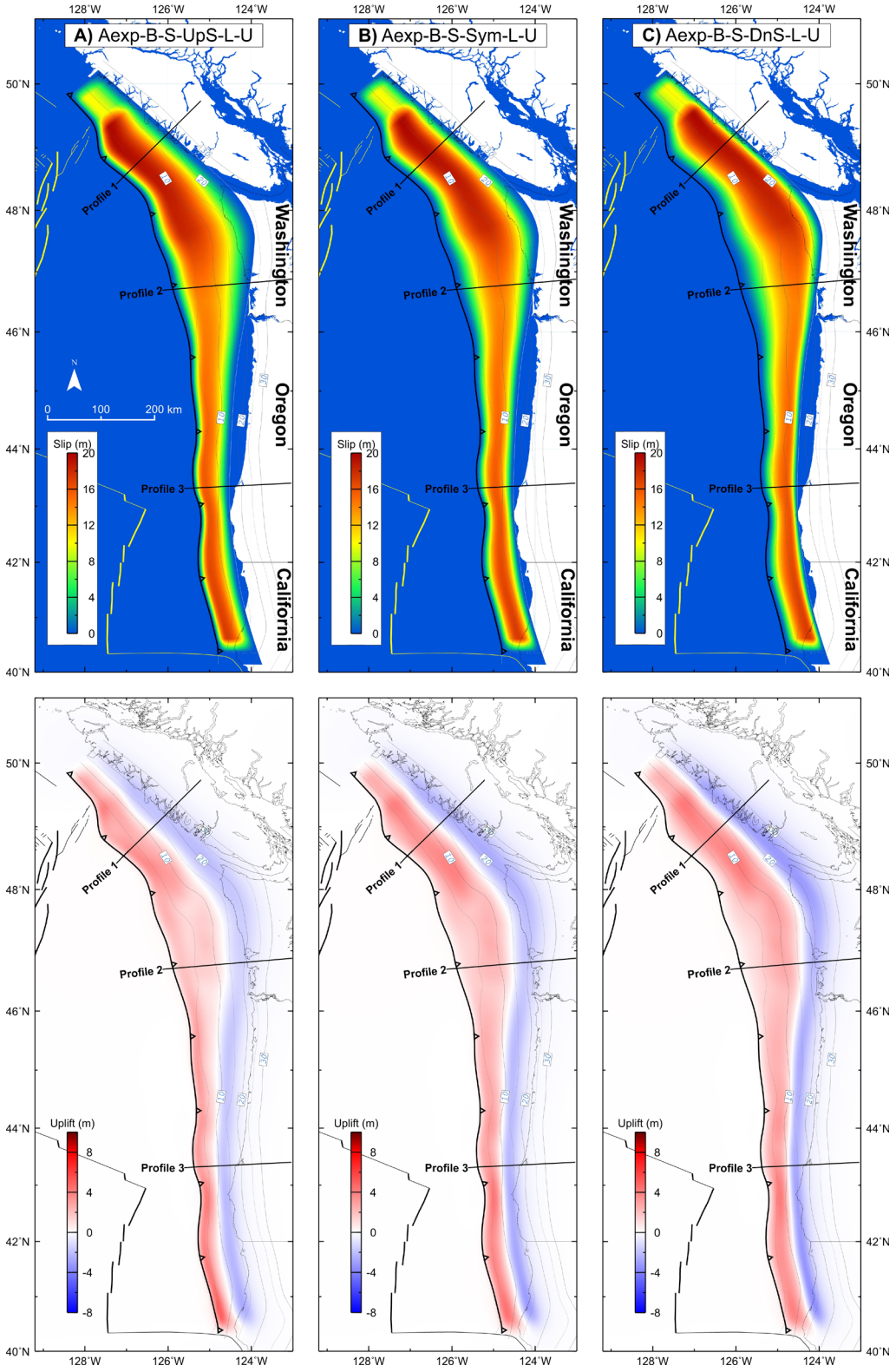

Figure 5.4. Surface deformation, fault slip, and fault geometry for profiles 1 to 3 (from north to south) in Figure 5.3, showing results for up-skew (red lines), symmetric (black lines), and down-skew (blue lines) whole margin shallow buried scenarios.

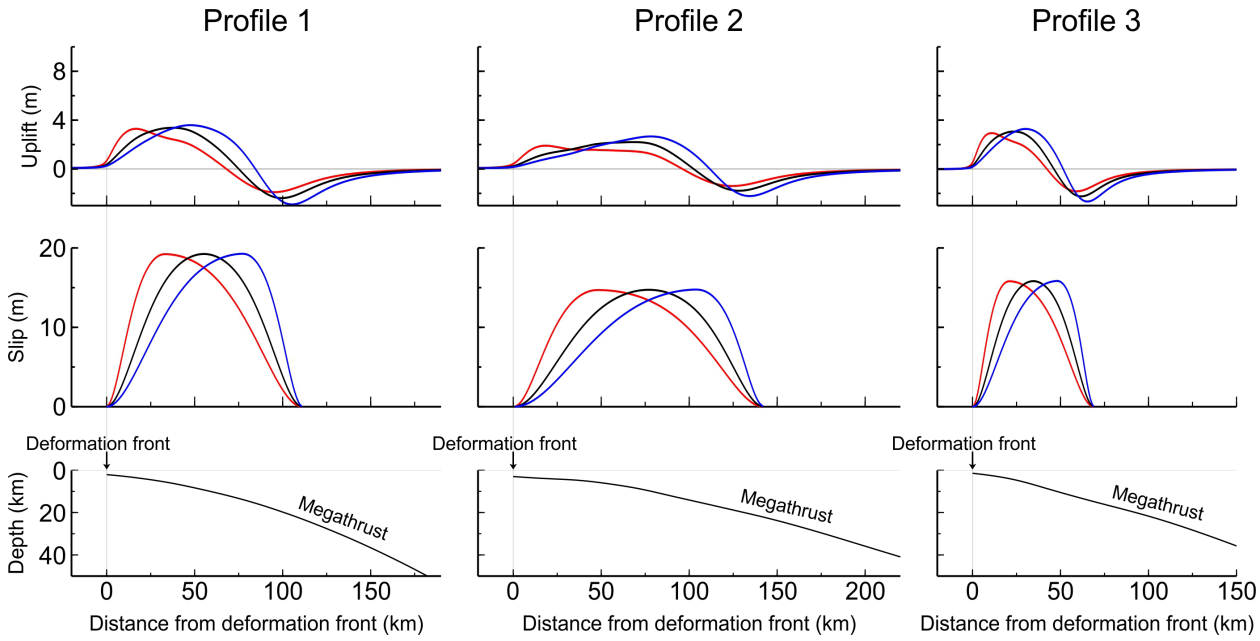

Figure 5.5. Examples of the slip of distribution (upper panel) and vertical deformation (lower panel) of whole-margin buried rupture with the three different down-dip rupture extent models: (A) M, Midpoint locked and 1 cm locked, (B) L, Locked zone and (C) T, Tremor downdip limits as defined in Figure 4. 3. These three examples use shallow buried rupture (B-S) and a symmetric (Sym) bell slip distribution. Model scenario names included at top of figure.

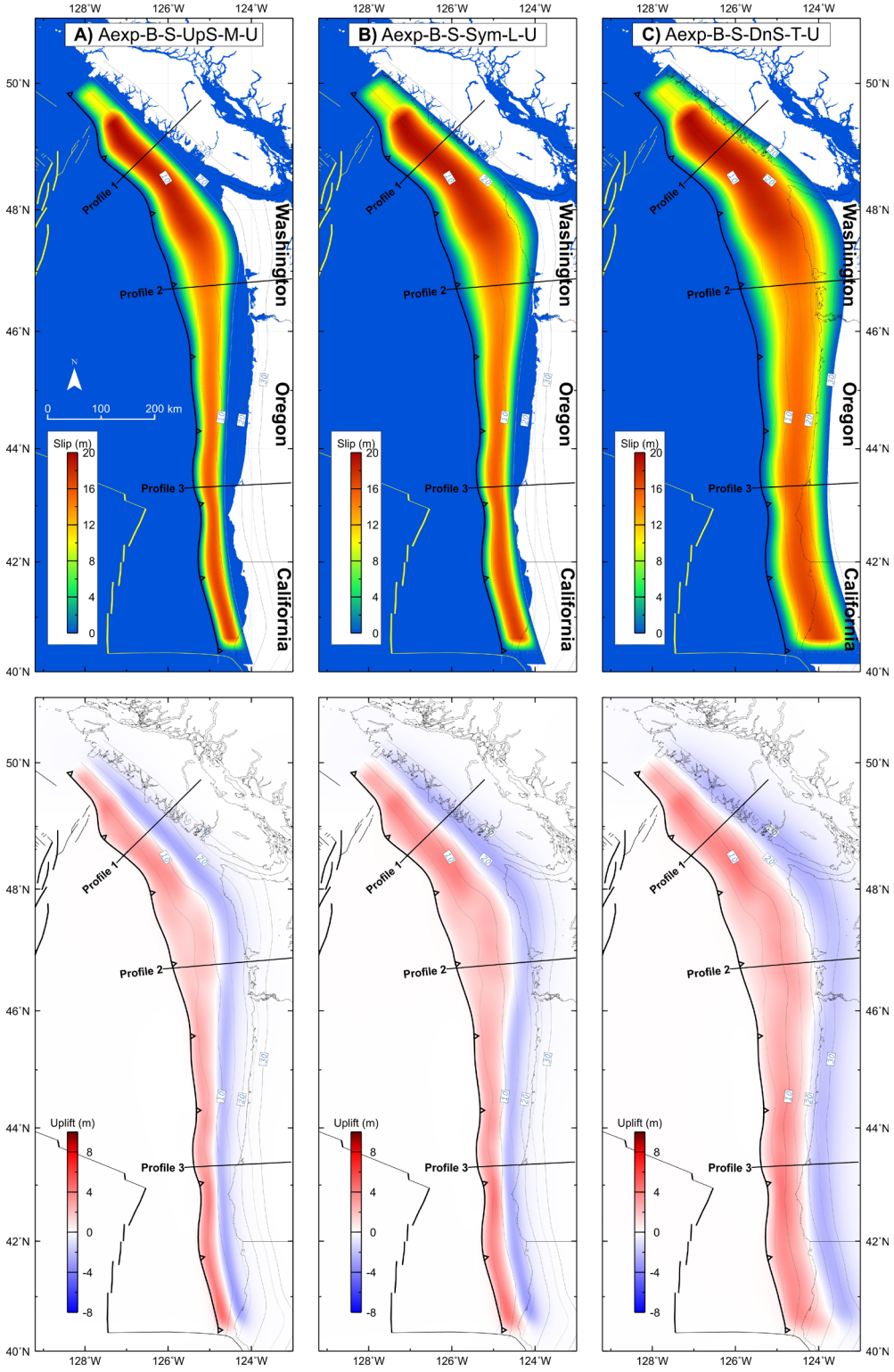

Figure 5.6. Surface deformation, fault slip, and fault geometry for profiles 1 to 3 (from north to south) in Figure 5.5, showing results for the Midpoint locked and 1 cm locked (M, red lines), Locked zone (L, green lines) and Tremor (T, purple lines) downdip limits.

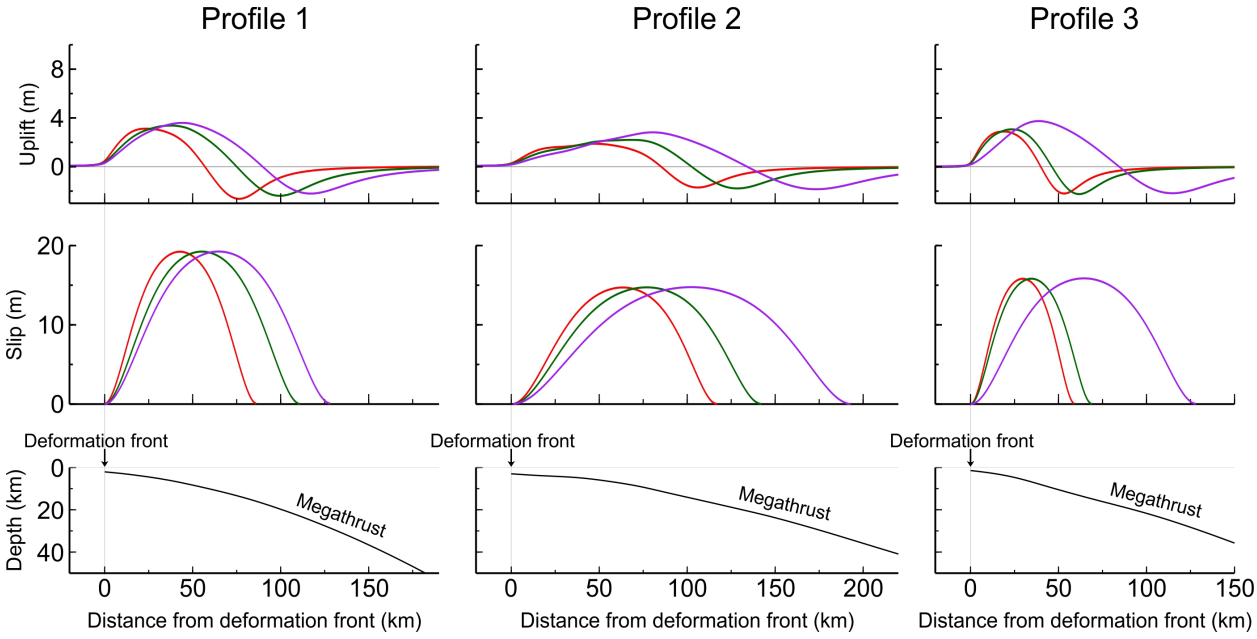

Figure 5.5 and **Figure 5.6** show how the downdip rupture limit affects deformation wavelength. Given the same peak slip, as the rupture zone widens due to a deeper limit, there is a corresponding increase in the deformation wavelength. For the symmetric slip distribution used here, the deepest one of the three downdip limits (**Figure 4. 3**) predicts little coastal subsidence or event uplift (**Figure 5.5c**). This is less consistent with paleoseismic observations for the 1700 CE earthquake (e.g., Wang and others, 2013), though we have less information for earlier paleoearthquakes. Needless to say, one can add a long tail of low-magnitude slip to extend the slip distributions shown in **Figure 5.5** to much greater depths without substantially altering the characteristics of their offshore and coastal deformation. The thermally controlled rheology has not yet been assessed to evaluate the validity of very deep megathrust rupture, nor to consider whether it has been observed in similarly warm subduction zones such as Nankai and Mexico (Hyndman and others, 1995; Wang and Trehu, 2016; Gao and Wang, 2017; Wang and others, 2024).

5.2 Whole-Margin Splay-Faulting Rupture

As discussed in Section **2.2**, splay-fault models B and D evolve from a splay-fault model initially suggested off of the Oregon coast by Priest and others (2010). As explained in Section **3.4**, for splay-faulting scenarios we map the bell-shaped slip distribution for the buried rupture onto the splay-fault geometry (**Figure 3.6c** and **Figure 5.8b**). Because splay faulting is assigned a very low weight in the updated logic tree (**Figure 4.1**), it suffices to include only the symmetric ($q = 0.5$) bell-shaped slip without subdividing the branch for variable skewness.

Figure 5.7. Examples of the slip of distribution (upper panel) and vertical deformation (lower panel) from the whole-margin splay-faulting rupture for (A) Splay B and (B) Splay D. Both these examples use the Sym slip distribution and the L downdip limit. Model scenario names included at top of figure.

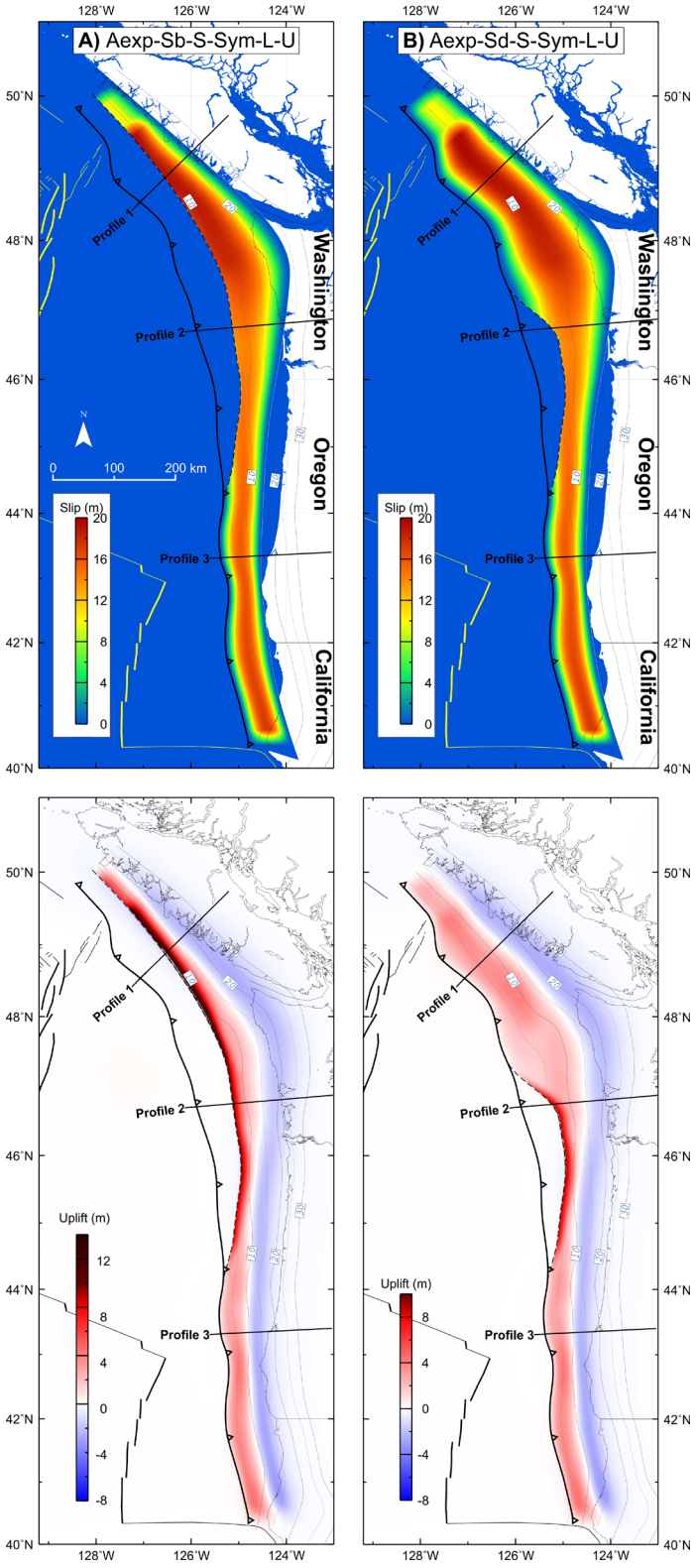

Figure 5.8. Surface deformation, fault slip, and fault geometry for profiles 1 to 3 (from north to south) in Figure 5.7 showing results for the Splay B (black lines) and Splay D (blue lines) scenarios.

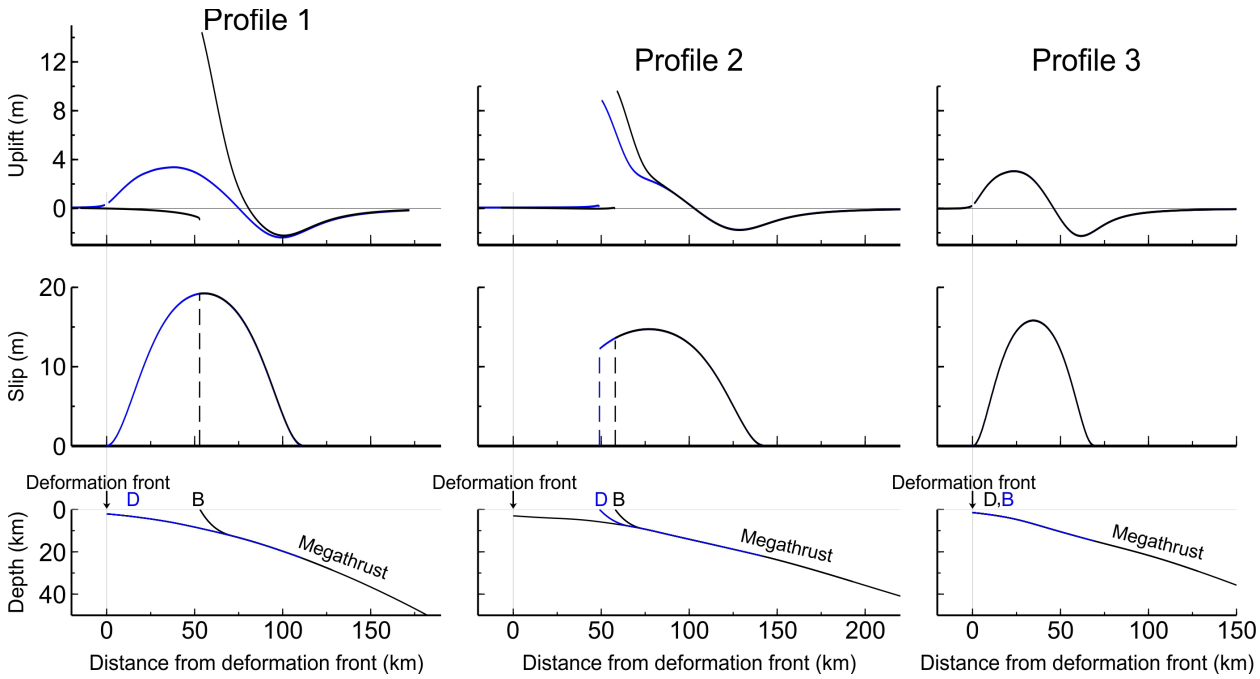

Both Splay B and Splay D scenarios feature large uplift near the fault traces due to their much greater dip than the megathrust. The similar or identical fault geometry between the two splay faults south of ~46°N lead to similar or identical deformation in this region (**Figure 5.7** and **Figure 5.8c**). Splay B would result in much greater seafloor uplift in northern Cascadia (**Figure 5.7** and **Figure 5.8a**), but CASIE21 imaging did not yield direct evidence for its presence in northern Cascadia (Section **2.2**).

5.3 Whole-Margin Trench-Breaching Rupture

The trench-breaching rupture scenarios for the logic tree include only up-skew (**Figure 3.7a**) and symmetric (**Figure 3.6b**) slip distributions for the deeper portion of rupture. The CSWG concluded that it is unlikely for the down-skewed slip to trigger trench-breaching shallow slip. As explained in Section 3.4 (**Figure 2.5**), our trench-breaching scenario includes a section of up-skewed buried rupture off of the Washington coast (**Figure 5.9,** upper panels).

Figure 5.9a and **Figure 5.9b** show the slip distribution and surface deformation for 50% peak slip breaching the trench with the deeper part of the slip being up-skewed and symmetric, respectively. **Figure 5.9c** and **Figure 5.9d** show similar relations for 100% trench breaching scenarios. The two trench-breaching scenarios included in the logic tree are meant to cover the uncertainties for the mechanical behavior of the shallow megathrust. An increased coseismic slip at the deformation front could imply a reduction in coseismic strengthening (Hu and Wang, 2008; Wang and He, 2008) or an enhancement in dynamic weakening (Di Toro and others, 2011; Noda and Lapusta, 2013). See Wang and others (2024) for further discussion.

Figure 5.9. Examples of whole-margin trench-breaching scenarios, including the area that lacks evidence for seaward vergence faulting off of the Washington coast. 50% (T50) peak slip breaches the model surface with (A) symmetric (Sym), and (B) up-skew (UpS) slip distribution for the lower downdip rupture extent. Equivalent 100% (T100) peak slip breaches are shown for (C) symmetric and (D) up-skew slip distributions. Model scenario names included at top of figure.

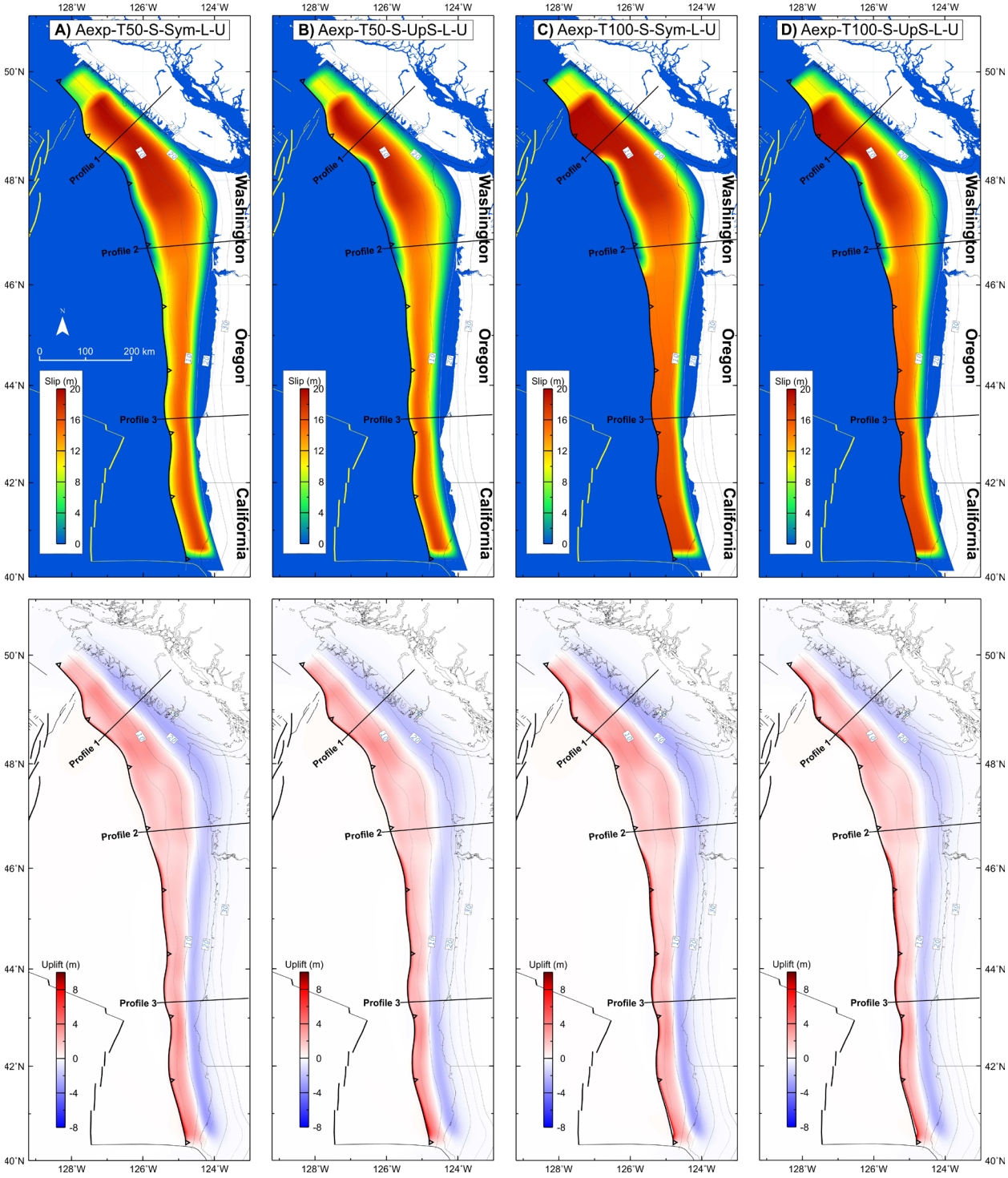

Except for off of the coast of Washington, our trench-breaching ruptures amplify uplift near the deformation front because large slip occurs on the steeply dipping frontal thrust (**Figure 5.10a** and **Figure 5.10c**). Just landward of the area of significant uplift at the frontal thrust, the uplift is reduced compared to scenarios involving buried ruptures (**Figure 5.2a** and **Figure 5.2c**). When the slip does not taper to the trench, there is less horizontal shortening of the upper plate, which moderates the vertical expansion. Unless the sediment cover hosting the frontal thrust is very think, on the order of 5 km (Carvajal and others, 2022), this effectively offsets the potential tsunami impact of increased uplift due to the frontal thrust (Gao and others, 2018).

Figure 5.10. Surface deformation, fault slip, and fault geometry for profiles 1 to 3 (from north to south) in Figure 5.9. For profile 1 or profile 3, the frontal thrust is present, and their middle panel shows the slip distribution with 50% (blue lines) and 100% (red lines) peak slip breaching the model surface. For profile 2 in the segment of no frontal thrust, the middle panel shows the up-skewed buried slip. For all the three profiles, solid and dashed lines depict up-skewed and symmetric slip distributions, respectively, and bell-shaped slip distribution in the deeper part of the rupture as explained in the second-last paragraph of Section 3.4.

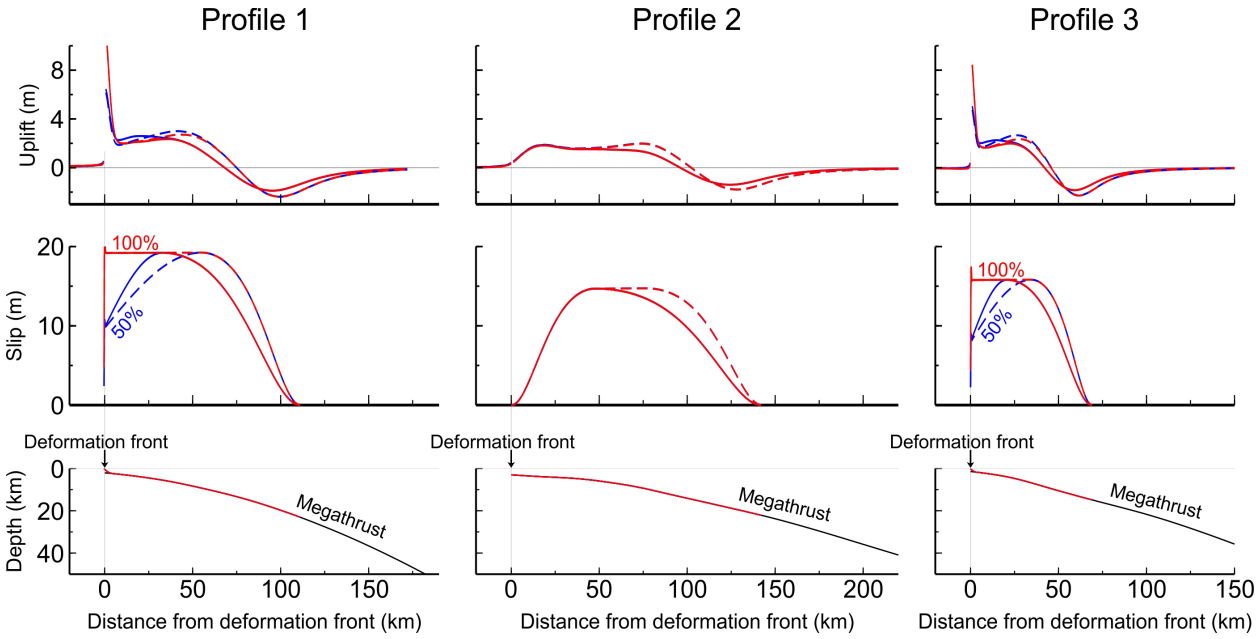

5.4 Asperity Models

In the asperity scenarios, one segment of the fault (the "asperity") experiences more slip than the rest of the fault, but the total moment of the simulated earthquake is the same as that produced by averaged slip distributed uniformly along strike. Recall (Section **4.0**) that by "uniform slip," we mean, "uniform period of slip deficit accumulation." For wording convenience, we continue to use the word slip with this meaning below. The asperity scenarios do not play an important role in the logic tree. Only a few of them were constructed and only for whole-margin ruptures.

We divided the margin into n segments of equal length in the strike direction and assign one of them to be the high-slip "asperity" and the other $n-1$ segments to have a uniform "background" slip. If we require the asperity segment to slip twice as much as the average slip of the n segments, the ratio of the background slip of the $n-1$ nonasperity segments (b) to the average slip of the n segments (a) is given by

$$\frac{b}{a} = \frac{n-2}{n-1} \tag{4}$$

Therefore, the background slip is simply $(n-2)/(n-1)$ times the average slip. For example, for $n = 3$, the background slip is half the average, and for $n = 5$, the background slip is 75% of the average slip. Similar to the uniform-slip whole-margin models described in Sections 5.1 – 5.3, each asperity model includes many scenarios with different rupture boundaries and slip distributions in the dip direction.

We create three asperity models for the DOGAMI whole-margin ruptures using $n = 3$. Examples are shown in **Figure 5.11** using symmetric shallow buried ruptures. The segment boundaries are straight lines in the dip direction in the Cartesian rectangular mesh (**Figure 3.5b**). After being mapped to the 3-D mesh (**Figure 3.5a**), they are slightly curved and may not be exactly margin-normal (**Figure 5.11**). In the 3-D mesh, each line centers a 25-km-wide zone of transition over which the slip linearly tapers from one value to another (e.g., from the high slip in the asperity to the background slip in the next segment).

We created five asperity models for USGS whole margin rupture using $n = 5$. In these models, the slip of the asperity segment tapers along strike much more gradually, following a sinusoidal function as illustrated in **Figure 5.12**. Examples are shown in **Figure 5.13** using symmetric shallow buried ruptures.

6.0 PARTIAL RUPTURE SCENARIOS

6.1 Segmented Tsunami Source Models

The along-strike "segmentation" in this category of models, illustrated in **Figure 4.2**, is slightly modified from Goldfinger and others (2017) following discussions with the CSWG. To account for uncertainties in the location of the segmentation boundaries, each boundary has two additional versions, being located north and south by approximately 50 km (grey boundary lines in **Figure 4.2**). The models that are 50 km north and south give rise to the "long" and "short" branches of the logic tree. Each boundary centers a 25-km-wide zone of transition over which the slip tapers to zero. We exclude the "E" scenario in Goldfinger and others (2017) due to it having a similar length to "D short." Except for segment F, all the segments share the same southern boundary at the MTJ. The logic tree is designed to reflect that the shorter segments farther south have more frequent ruptures with smaller slip. Similar boundaries were used by Witter and others (2011) but in a different way, as discussed in Section **5.0**.

Accordingly, when one of the segments in **Figure 4.2** ruptures, the rest of the margin does not. However, just like for whole-margin rupture, each segment rupture includes all the scenarios described in Sections **5.1** – **5.4**, encompassing different variations in the dip direction and the asperity model. For the segment rupture asperity models, we only have the $n = 3$ option, similar to those shown in **Figure 5.11**, but for shorter rupture lengths.

Figure 5.11. Examples of the DOGAMI whole-margin *n* = 3 asperity models. Models of (A) northern, (B) center, and (C) southern asperity are shown respectively. Each of these examples use the Sym shallow buried rupture and the L downdip limit. Model scenario names included at top of figure.

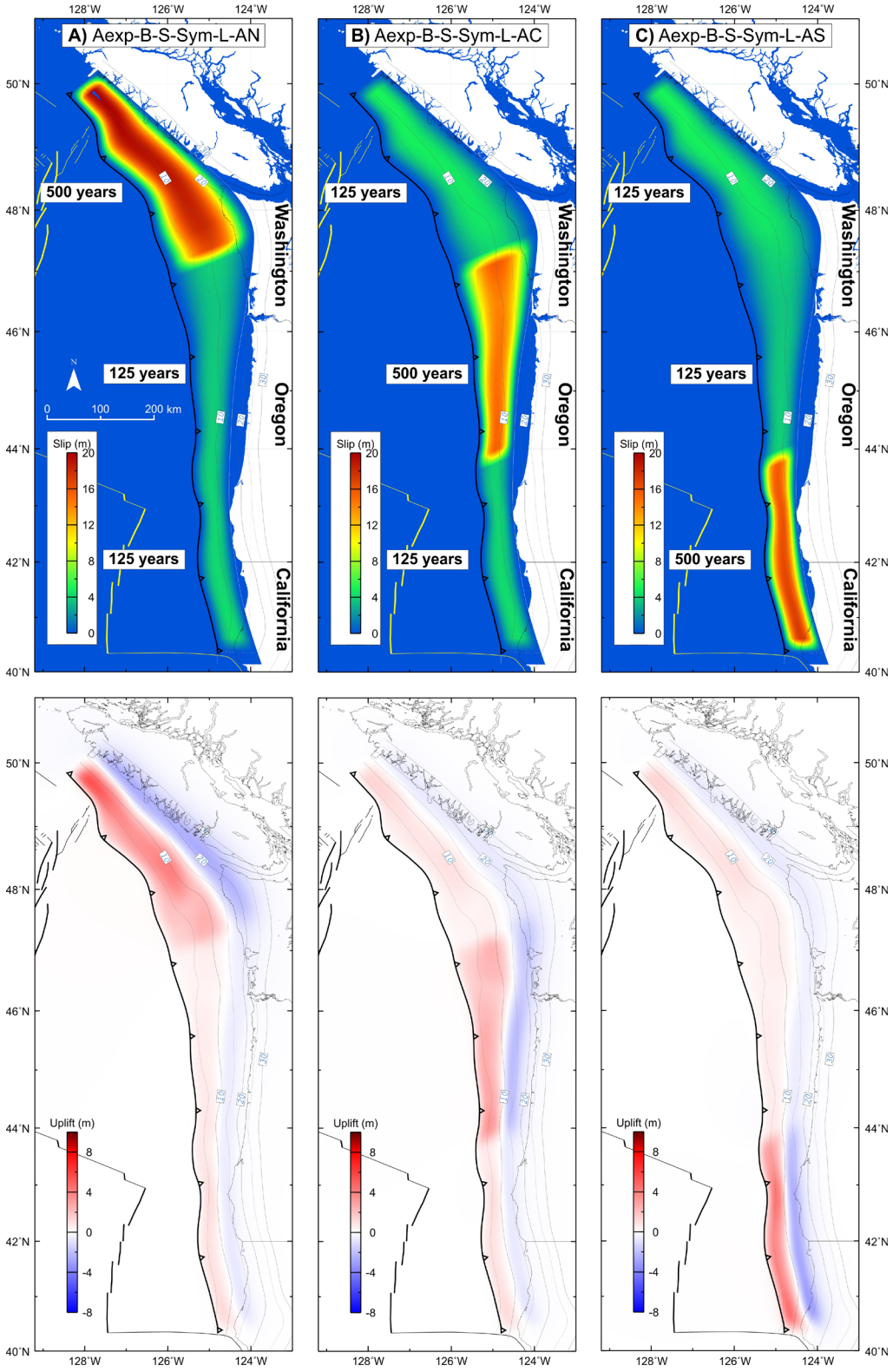

Figure 5.12. Illustration of the along-strike variations of slip in the five USGS asperity models. The shape function is applied in the Cartesian rectangular mesh, as shown here, and is then mapped to the 3-D curved mesh, as shown in the top row of Figure 5.13.

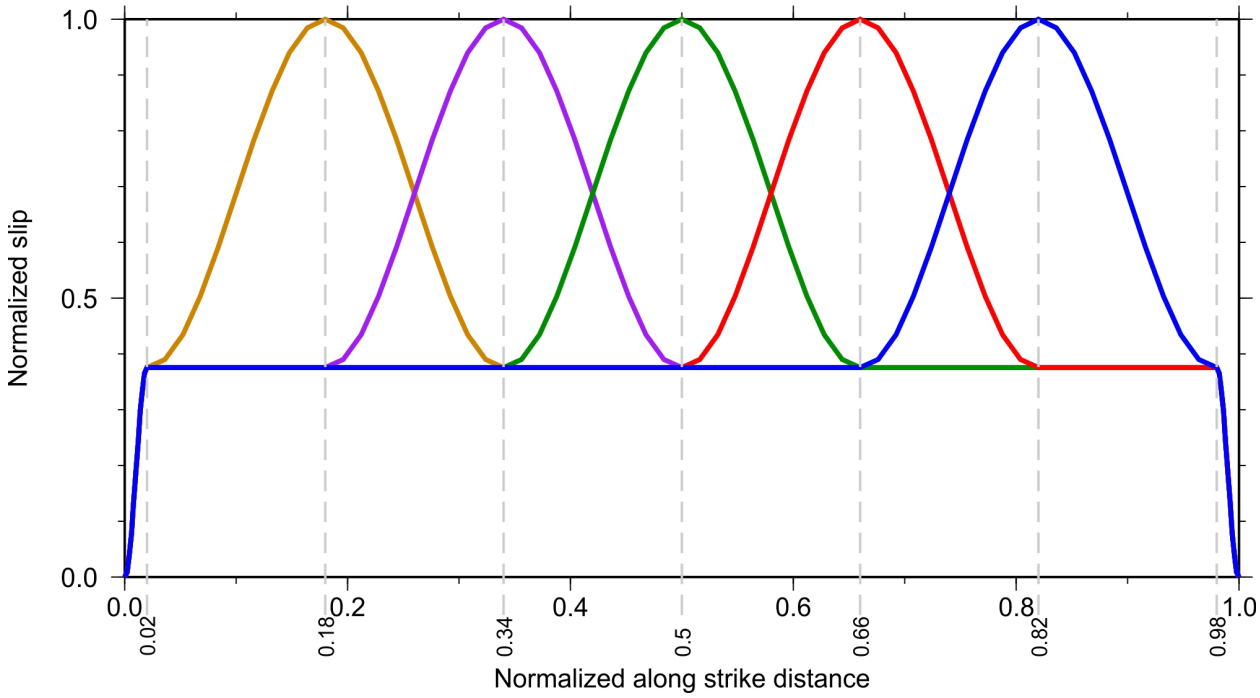

Figure 5.13. Examples of the whole-margin *n* = 5 asperity models. Slip variation in the strike direction for each model is shown in Figure 5.12. These five examples use the Sym shallow buried rupture and the L downdip limit. Model scenario names included at top of figure.

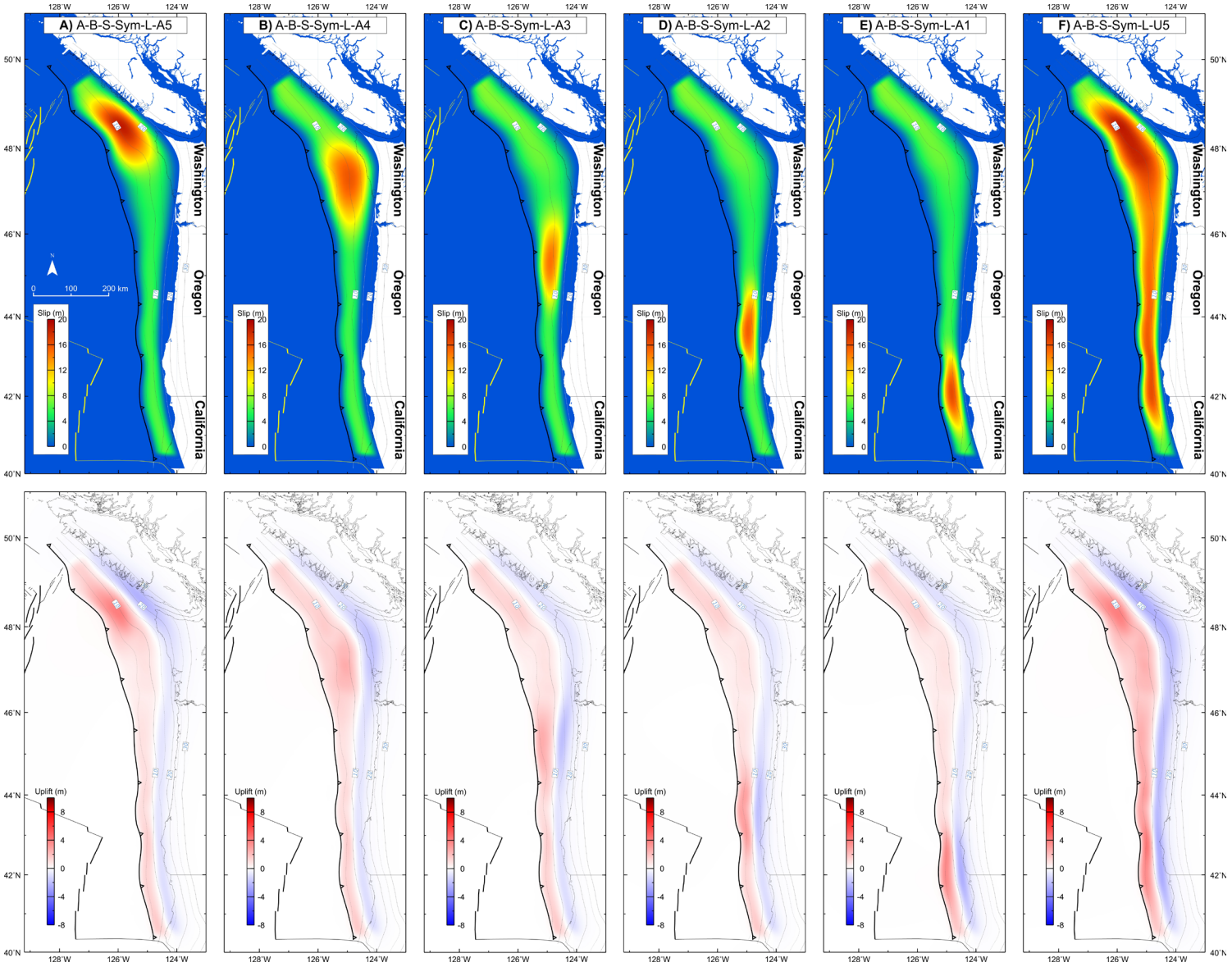

6.2 Cluster M8 Tsunami Source Models

Further under the USGS branch we have a subset of the "cluster" category scenarios, which has a wide range of along-strike rupture lengths and locations of termination (**Figure 6.1**). The definition of these cluster segments is from the USGS NSHM. Four large sections were first defined as shown in **Figure 6.1**. These are then further subdivided into nine sections spanning the regions between Nehalem Bank–Vancouver Island, three sections between Heceta Bank–Nehalem Bank, three sections between Cape Blanco–Heceta Bank, and seven sections between Mendocino–Cape Blanco. Subdivisions are combined to form rupture segments at five levels (**Figure 6.1**), in which level 3 has two options. Different from the segments shown in **Figure 4.2**, the north and south boundaries of the cluster segments do not have the additional ± 50 km variations and their segments do not share a common southern boundary. The north or south boundary of each rupture centers a 25-km-wide zone of transition over which the slip linearly tapers to zero.

Figure 6.2 shows an example of the suite of five-level clusters using the symmetric shallow buried rupture. Similar to the whole-margin and segmented categories, each of the rupture models in the cluster category includes many scenarios with different rupture boundaries and slip distributions in the dip direction (see Sections **5.1**–**5.3**). The asperity models are not used for the cluster segments.

6.3 Floating Tsunami Source Models

In the floating rupture category, the same sized rupture patch slips in different locations along the margin for different scenarios. Floating ruptures are considered in the USGS NSHM. In the present study, the decision was made by the CSWG to use a 100 km by 40 km elliptical patch in which the slip peaks in the middle and tapers in all directions, as shown in **Figure 3.8**a. The CSWG also decided that the floating models only involve the megathrust, without the splay or frontal-thrust geometry. With the fixed rupture dimension, the various rupture boundaries shown in **Figure 3.8** are not needed. We constructed 10 models of this type, as illustrated in **Figure 6.3**. The ellipses are manually adjusted so that the updip edge is as close to the deformation front as possible. The slip distribution and the surface deformation of these 10 models are shown in **Figure 6.4**.

Figure 6.1. Definition of the five-level cluster ruptures based on the cluster setup in the USGS NSHM.

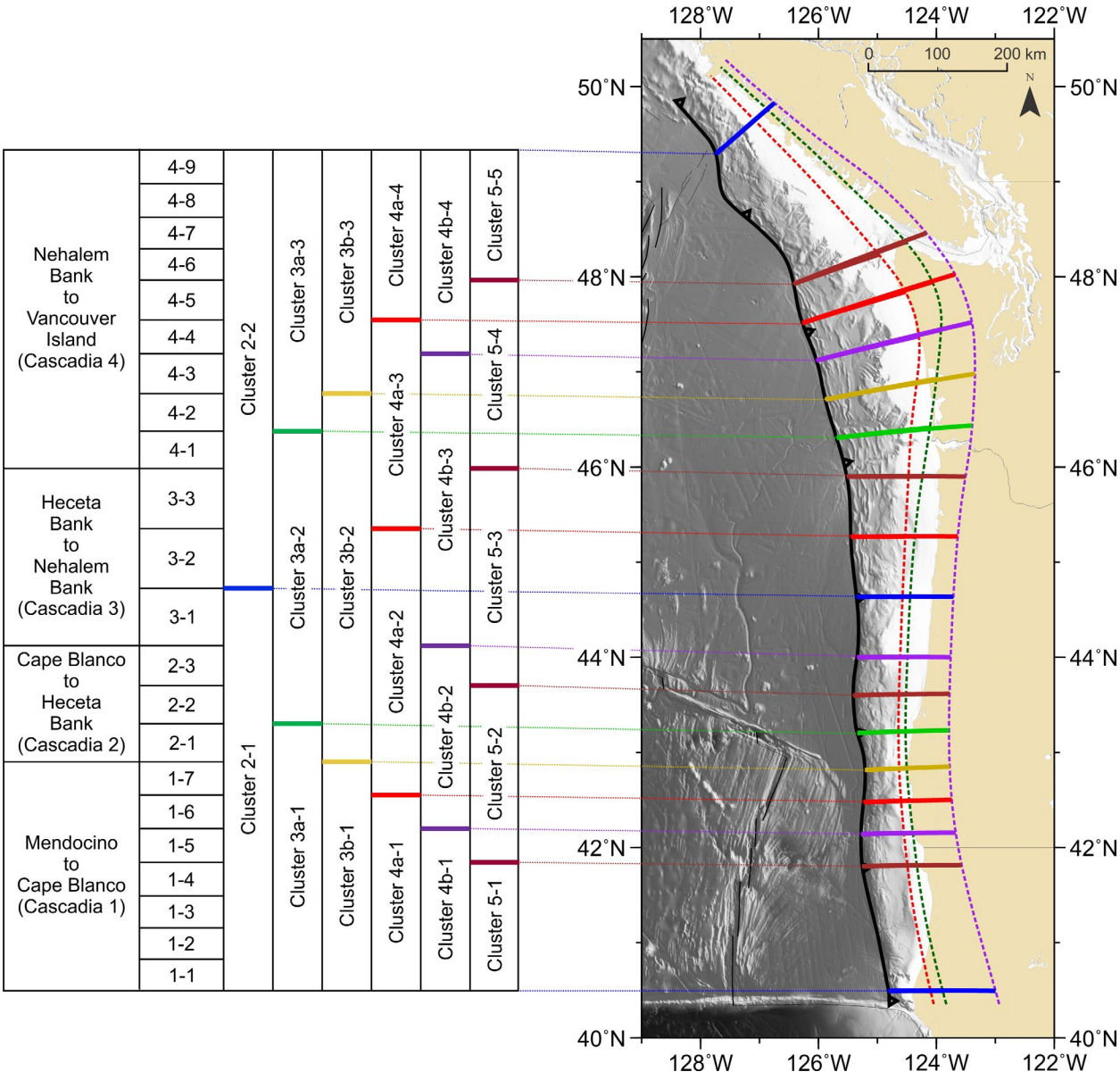

Figure 6.2. Examples of the five-level cluster ruptures. The along-strike boundaries are defined in Figure 6. 1. This example uses the Sym shallow-buried rupture with the L downdip limit.

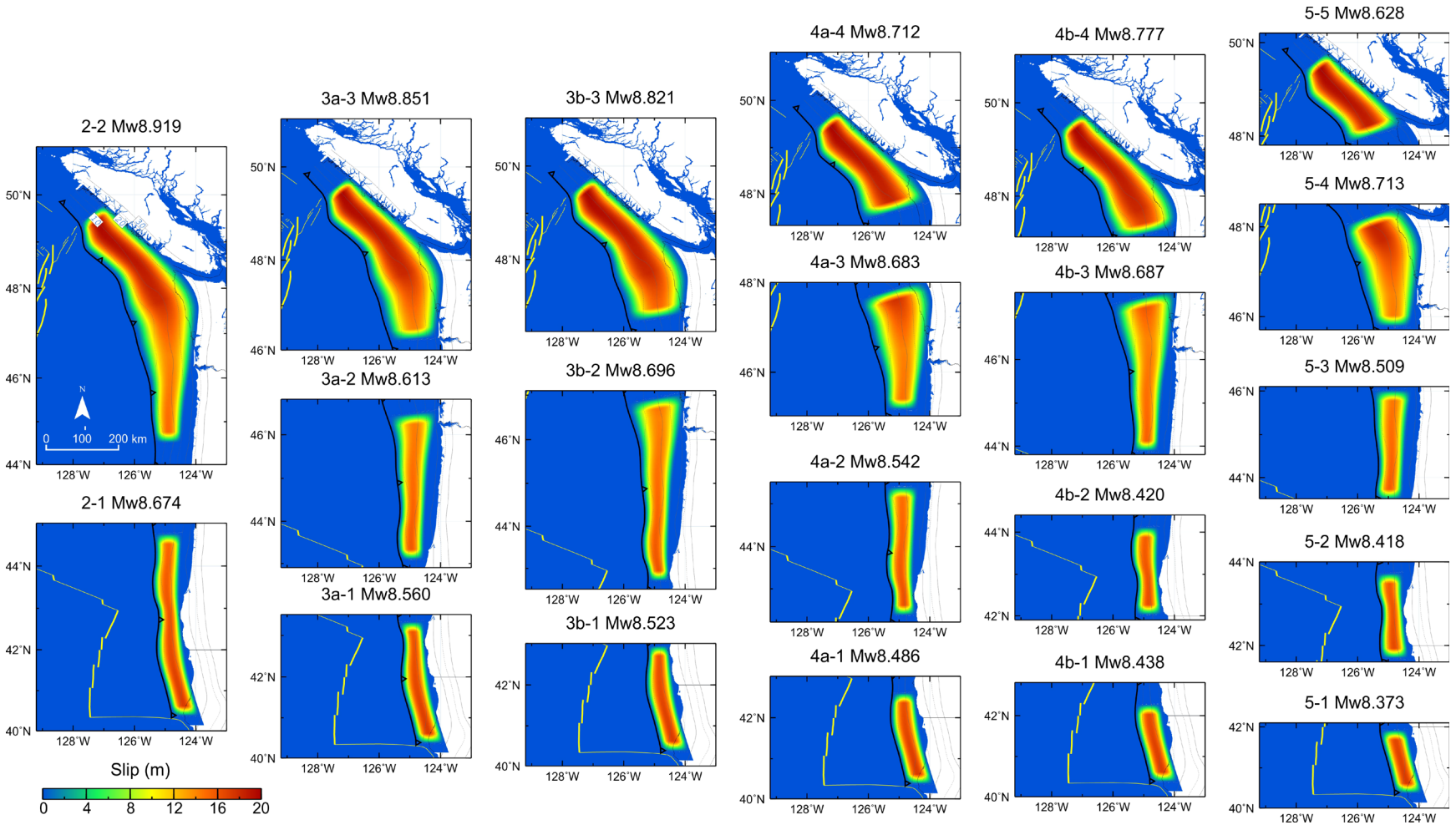

Figure 6.3. Floating rupture boundaries. The use of red and blue colors is only for display clarity with no other significance. All the ruptures are elliptical and of the same size in map view.

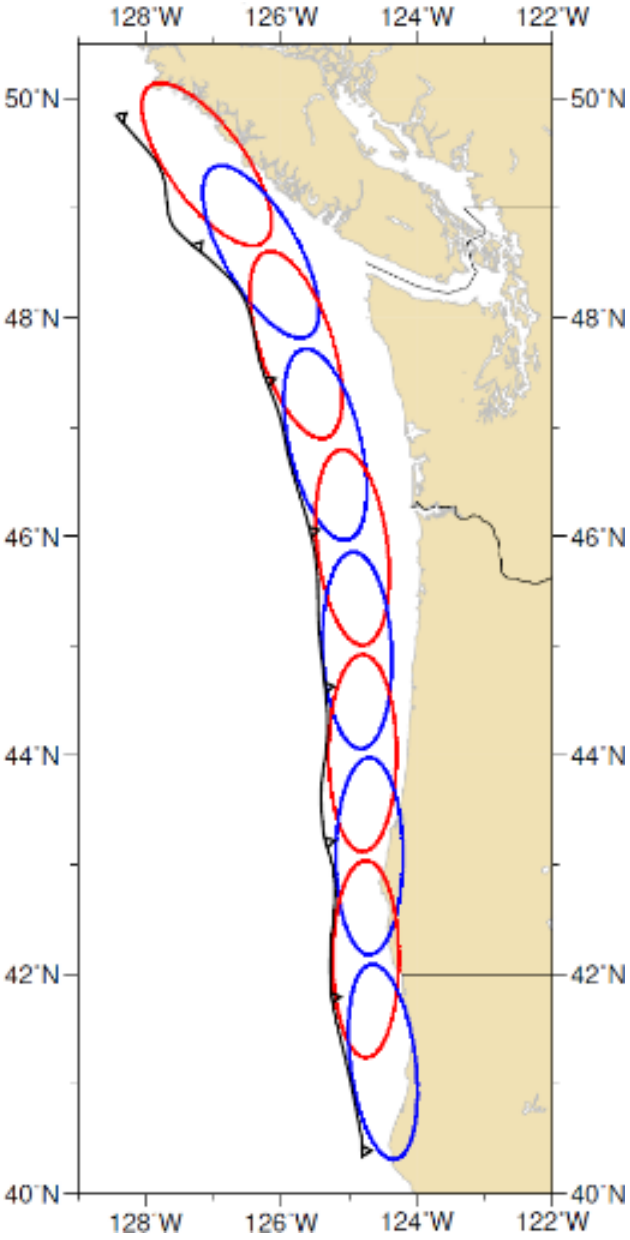

Figure 6.4. Slip distribution (upper) and surface vertical deformation (lower) for all ten elliptical floating-rupture patch scenarios. The ruptures have the same area in map view, but the earthquake magnitude varies because the maximum slip derived from the Euler vectors (Section 3.4) varies along strike.

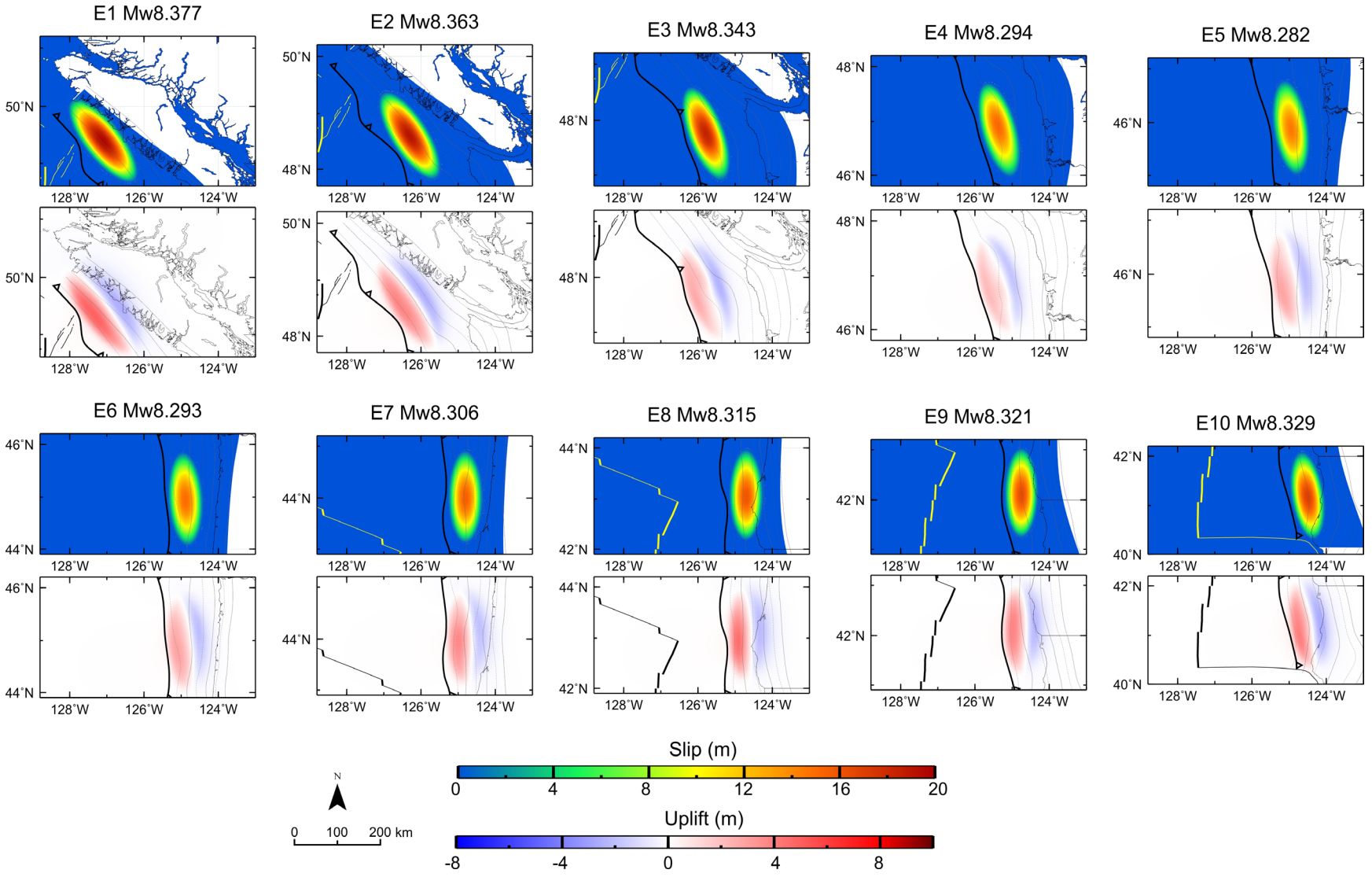

7.0 CONCLUSION

This Cascadia Earthquake Source Models for Tsunami Hazard Assessments report presents a comprehensive update and refinement of tsunami source scenarios for the CSZ, incorporating a suite of 3,502 models developed through integration of new seismic imaging data, updated geological interpretations, and advanced modeling techniques. The objective of this study was to produce the next-generation Cascadia earthquake source models, which will be used as input for the next generation of tsunami hazard modeling to be performed in Cascadia. Aimed at improving on the previous PTHA undertaken by the American Society of Civil Engineers in 2016, this study marks a significant step forward in our understanding of the tsunami risks associated with the CSZ. Guided by the logic tree methodology, the study systematically evaluates a suite of potential tsunami sources. The logic tree framework is instrumental in structuring the exploration of uncertainties in seismic source parameters, thereby enabling a comprehensive assessment of the tsunami hazards posed by the CSZ.

The report's utilization of the logic tree includes a detailed consideration of multiple rupture scenarios, encompassing variations in rupture length, slip distribution, and rupture type, among other factors. This allows for a broad representation of possible tsunami sources. Technical expertise and the latest scientific data were used to define parameters and probabilities to different branches of the tree, ensuring that the model reflects the current understanding of Cascadia while also accounting for uncertainties.

Future enhancements to the Cascadia model will focus on integrating a more precise depiction of the megathrust in some regions, including near the MTJ where research is ongoing to reanalyze and reprocess seismic profiles. Additionally, the study highlights the necessity to bridge the substantial gap in low-frequency earthquake data between California and Washington, pinpointing a key opportunity for future research to deepen our comprehension of the megathrust geometry.

In conclusion, this report offers a substantial improvement in Cascadia sources models that will guide future tsunami hazard modeling throughout the region. It lays a foundation for continued research and collaboration in the field, highlighting areas where further studies are needed to refine our understanding of Cascadia's tsunami potential.

8.0 ACKNOWLEDGMENTS

This project was funded as subaward IA DOGAMI EOSU 22-922 by the Oregon Department of Geology and Mineral Industries as part of award NA21NWS4670010 by NOAA through the National Tsunami Hazard Mitigation Program.

This project was the vision of DOGAMI staff to help develop updated Cascadia earthquake source models that could be used to develop the next generation of regional tsunami models. To facilitate this process, a small working group of experts from diverse backgrounds assisted Matthew Sypus in constructing all the various scenarios in the suite. Experts included staff from DOGAMI, USGS, AECOM, Washington Department of Natural Resources, Oregon State University, California Geological Survey, University of Washington, and the University of Victoria. Core members of the CSWG are listed before the Abstract.

The CASIE21 team provided critical new data for the shallow geometry of the megathrust. The Ad hoc Working Group for Synthesizing Legacy Seismic Data for Southern Cascadia off of California (listed before the Abstract) provided updated information on megathrust geometry off of California.

The authors greatly appreciate the many constructive review comments provided by Drs. Jonathan Allan and Reed Burgette (DOGAMI), Dr. Jay Patton with the California Geological Survey, and Dr. Diego Melgar (University of Oregon).

9.0 REFERENCES

Beaudoin, B. C., Godfrey, N. J., Klemperer, S. L., Lendl, C., Tréhu, A. M., Henstock, T. J., Levander, A., Holl, J. E., Meltzer, A. S., Luetger, J. H., and Mooney, W. D., 1996, Transition from slab to slabless: Results from the 1993 Mendocino triple junction seismic experiment. *Geology, 24*(3), 195–199. doi:10.1130/0091-7613

Brown, L., Wang, K., and Sun, T., 2015, Static stress drop in the Mw 9 Tohoku-oki earthquake: Heterogeneous distribution and low average value, *Geophysical Research Letters, 42*, 10,595–10,600, doi:10.1002/2015GL066361.

Carbotte, S., Boston, B., Han, S., Shuck, B., Beeson, J., Canales, J. P., and others, 2024, Subducting plate structure and megathrust morphology from deep seismic imaging linked to earthquake rupture segmentation at Cascadia. *Science Advances*, 10, eadl3198.

Carvajal, M., Sun, T., Wang, K., Luo, H., and Zhu, Y., 2022, Evaluating the tsunamigenic potential of buried versus trench-breaching megathrust slip. *Journal of Geophysical Research: Solid Earth*, *127*, e2021JB023722. doi:10.1029/2021JB023722

Di Toro, G., Han, R., Hirose, T., De Paola, N., Nielsen, S., Mizoguchi, K., and others, 2011, Fault lubrication during earthquakes. *Nature* 471(7339), 494–498. doi:10.1038/nature09838

Flück, P., Hyndman, R. D., and Wang, K., 1997, Three-dimensional dislocation model for great earthquakes of the Cascadia Subduction Zone, *Journal of Geophysical Research*, *102*(B9), 20539–20550. doi:10.1029/97JB01642

Frankel, A., Chen, R., Petersen, M., Moschetti, M., and Sherrod, B., 2015, 2014 update of the Pacific Northwest portion of the US National Seismic Hazard Maps. *Earthquake Spectra,* 31(1_suppl), S131-S148. doi:10.1193/111314EQS193M

Freund, L.B., and D.M. Barnett, 1976, A two-dimensional analysis of surface deformation due to dip-slip faulting. *Bulletin of the Seismological Society of America*, 66, 667–675.

Gao, D., 2016, *Defining Megathrust Tsunami Sources at Northernmost Cascadia Using Thermal and Structural Information* (Master's Thesis). Victoria, BC: University of Victoria. Retrieved from http://hdl.handle.net/1828/7435

Gao, D., Wang, K., Davis, E. E., Jiang, Y., Insua, T. L., and He, J., 2017, Thermal state of the Explorer segment of the Cascadia subduction zone: Implications for seismic and tsunami hazards. *Geochemistry, Geophysics, Geosystems, 18*(4), 1569–1579. doi:10.1002/2017GC006821

Gao, D., Wang, K., Insua, T. L., Sypus, M., Riedel, M., and Sun, T., 2018, Defining megathrust tsunami source scenarios for northernmost Cascadia. *Natural Hazards, 94*(1). doi:10.1007/s11069-018-3397-6

Gao, X. and Wang, K., 2017, Rheological separation of the megathrust seismogenic zone and Episodic Tremor and Slip, *Nature*, *543*, 416–419, 10.1038/nature21389.

Goldfinger, C., Galer, S., Beeson, J., Hamilton, T., Black, B., Romsos, C., Patton, J., Nelson, C. H., Hausmann, R., and Morey, A., 2017, The importance of site selection, sediment supply, and hydrodynamics: A case study of submarine paleoseismology on the northern Cascadia margin, Washington, USA. Marine *Geology, 384*, 4–46. doi:10.1016/j.margeo.2016.06.008

Goldfinger, C., Nelson, C., Morey, A., Johnson, J., Patton, J., Karabanov, E., Gutiérrez-Pastor, J., Eriksson, A. T., Gràcia, E., Dunhill, G., Enkin, R. J., Dallimore., A., and Vallier, T., 2012, Turbidite event history: Methods and implications for Holocene paleoseismicity of the Cascadia subduction zone. *U.S. Geological Survey Professional Paper 1661-F*, 184 p. doi:10.3133/pp1661F

Gomberg, J., Bedrosian, B., Bodin, P., Bostock, M., Brudzinski, M., Creager, K., Dragert, H., Egbert, G., Ghosh, A., Henton, J., Houston, H., Kao, H., McCrory, P., Melbourne, T., Peacock, S., Roeloffs, E., Rubinstein, J., Schmidt, D., Tréhu, A., Vidale, J., Wang, Kelin, and Wech, A., 2010, Slow-slip phenomena in Cascadia from 2007 and beyond—A review: *Geological Society of America Bulletin, 122*(7-8), 963–978 doi:10.1130/B30287.1

Gulick, S. P. S., A. M. Meltzer, and S. H. Clarke Jr., 1998, Seismic structure of the southern Cascadia subduction zone and accretionary prism north of the Mendocino triple junction, *Journal of Geophysical Research*, *103*(B11), 27207–27222. doi:10.1029/98JB02526

Hayes, G. P., Moore, G. L., Portner, D. E., Hearne, M., Flamme, H., Furtney, M., and Smoczyk, G. M., 2018, Slab2, a comprehensive subduction zone geometry model. *Science*, 362(6410), 58–61. doi:10.1126/science.aat4723

Hyndman, R. D., Wang, K., and Yamano, M., 1995, Thermal Constraints on the Seismogenic Portion of the Southwestern Japan Subduction Thrust. *Journal of Geophysical Research, Solid Earth* 100 (B8), 15373-15392. doi:10.1029/95jb00153

Hu, Y. and Wang, K., 2008, Coseismic strengthening of the shallow portion of the subduction fault and its effects on wedge taper. *Journal of Geophysical Research, Solid Earth*, 113(B12), B12411-n/a. doi: 10.1029/2008JB005724

Hutchinson, J., Kao, H., Spence, G., Obana, K., Wang, K., and Kodaira, S., 2019, Seismic Characteristics of the Nootka Fault Zone: Results from the Seafloor Earthquake Array Japan–Canada Cascadia Experiment (SeaJade). *Bulletin of the Seismological Society of America,* 109(6), 2252–2276. doi:10.1785/0120190008

Ledeczi, A., Lucas, M., Tobin, H., Watt, J. and Miller, N., 2024, Late Quaternary Surface Displacements on Accretionary Wedge Splay Faults in the Cascadia Subduction Zone: Implications for Megathrust Rupture. *Seismica*, 2(4).

Ma, S., 2012, A self-consistent mechanism for slow dynamic deformation and tsunami generation for earthquakes in the shallow subduction zone, *Geophysical Research Letters*, 39, L11310, doi:10.1029/2012GL051854

McCrory, P. A., Blair, J. L., Oppenheimer, D. H., and Walter, S. R., 2006, Depth to the Juan De Fuca Slab Beneath the Cascadia Subduction Margin—A 3-D Model for Sorting Earthquakes. U.S. Geological Survey, U.S. Department of Interior. doi:10.3133/ds91

McCrory, P. A., Blair, J. L., Waldhauser, F., and Oppenheimer, D. H., 2012, Juan de Fuca slab geometry and its relation to Wadati-Benioff zone seismicity. *Journal of Geophysical Research: Solid Earth, 117*(9), B09306. doi:10.1029/2012JB009407

Merrill, R. J., Bostock, M. G., Peacock, S. M., Schaeffer, A. J., and Roecker, S. W., 2022, Complex structure in the Nootka Fault zone revealed by double-difference tomography and a new earthquake catalog. *Geochemistry, Geophysics, Geosystems, 23*(2), e2021GC010205. doi:10.1029/2021GC010205

Noda, H. and Lapusta, N., 2013, Stable creeping fault segments can become destructive as a result of dynamic weakening. *Nature*, 493(7433), 518–521. doi:10.1038/nature11703

Okada, Y., 1985, Surface deformation due to shear and tensile faults in a halfspace. *Bulletin of the Seismological Society of America*, 75, 1135– 1154

Okada, Y., 1992, Internal deformation due to shear and tensile faults in a half-space. *Journal of Geophysical Research, 82*(2), 1018–1040. doi:10.1029/92JB00178

Patton, J.R., Eble, M.C., Kyriakopoulos, C., Lynett, P.J., Nicolsky, D., Ross, S., Ryan, K.J., Thio, H.K. and Wilson, R.I., 2022, U.S. Geological Survey Tsunami Sources Powell Center Working Group: Cascadia Probabilistic Tsunami Hazard Assessment Meeting Summary, AGU Fall Meeting. American Geophysical Union, Chicago, Illinois.

Petersen, M.D., Moschetti, M.P., Powers, P., Mueller, C.S., Haller, K.M., Frankel, A.D., Zeng, Y., Rezaeian, S., Harmsen, S.C., Boyd, O.L., Field, N., Chen, R., Rukstales, K.S., Luco, N., Wheeler, R.L., Williams, R.A., and Olsen, A.H., 2014, Documentation for the 2014 national seismic hazard maps, *U.S. Geological Survey Open-File Report, 2014-1091*, pp. 255. doi:10.3133/ofr20141091

Peterson, M.D., Shumway, A.M., Powers, P.M., Field, E.H., Moschetti, M.P, and others, 2023, The 2023 US 50-State National Seismic Hazard Model: Overview and implications. *Earthquake Spectra*: 1-84.

Plourde, Alexandre P., Bostock, Michael G., Audet, Pascal, and Thomas, Amanda M., 2015, Low-Frequency Earthquakes at the Southern Cascadia Margin. *Geophysical Research Letters*, 42(12), 4849-4855. doi:10.1002/2015GL064363

Priest, G. R., Goldfinger, C., Wang, K., Witter, R. C., Zhang, Y., and Baptista, A. M., 2010, Confidence levels for tsunami-inundation limits in northern Oregon inferred from a 10,000-year history of great earthquakes at the Cascadia subduction zone. *Natural Hazards*, 54(1), 27–73. doi:10.1007/s11069-009-9453-5

Savard, G., Bostock, M. G., Hutchinson, J., Kao, H., Christensen, N. I., and Peacock, S. M., 2020, The Northern Terminus of Cascadia Subduction. *Journal of Geophysical Research: Solid Earth,* 125(6), e2019JB018453. doi:10.1029/2019JB018453

Savard, G., Bostock, M. G., and Christensen, N. I., 2018 Seismicity, Metamorphism, and Fluid Evolution Across the Northern Cascadia Fore Arc. *Geochemistry, Geophysics, Geosystems :* G3, 19(6), 1881–97. doi:10.1029/2017GC007417

Sypus, Matthew, 2019, *Models of tsunamigenic earthquake rupture along the west coast of North America* (Master's Thesis). Victoria, BC: University of Victoria. Retrieved from http://hdl.handle.net/1828/11436

Sypus, M., Wang, K., Carbotte, S.M., Trehu, A.M., Goldfinger, C., Tobin, H.J., Lucas, M.C., Ledeczi, A., Watt, J.T., Ross, S., Thio, H.K., Patton, J.R., Allan, J.C., Burgette, R.J., Allen, C., Han, S., Gulick, S.P.S., Boston, B., Schuck, B. and Zhu, Y., 2023, Improving Cascadia Tsunami Source Models for Hazard Assessment by Integrating Geophysical and Geological Observations, AGU23, San Francisco, California.

Tanioka, Y. and Satake, K., 1996, Tsunami generation by horizontal displacement of ocean bottom. *Geophysical Research Letters*, *23*(8), 861–864. doi:10.1029/96GL00736

Royer, A.A., 2014, *Studies of seismic deconvolution and low-frequency earthquakes* (PhD Thesis). Vancouver, BC: University of British Columbia. Retrieved from https://open.library.ubc.ca/soa/cIRcle/collections/ubctheses/24/items/1.0165914

Royer, A. A., and M. G. Bostock, 2014., A comparative study of low frequency earthquake templates in northern Cascadia, *Earth and Planetary Science Letters*, 402, 247–256.

Wang, K., Bilek, S.L., 2014, Fault creep caused by subduction of rough seafloor relief. *Tectonophys*. 610, 1–24.

Wang, K. and He, J., 2008, Effects of frictional behaviour and geometry of subduction. *Bulletin of the Seismological Society of America*, *98*(2), 571–579. doi:10.1785/0120070097

Wang, K. and Tréhu. A. M., 2016, Invited review paper: Some outstanding issues in the study of great megathrust earthquakes – the Cascadia example, *Journal of Geodynamics*, 98, 1–18. doi:10.1016/j.jog.2016.03.010.

Wang, K., Carvajal, M., Zhu Y., Sun, T., He., J., and Sypus, M., 2024, Chapter 8: Informing Megathrust Tsunami Source Models with Knowledge of Tectonics and Fault Mechanics. In: K. Goda, R. De Risi, A. Gusman and I. Nistor (Editors), *Probabilistic Tsunami Hazard and Risk Analysis Towards Disaster Risk Reduction and Resilience*. Elsevier, Netherlands, pp. 257-276.

Wang, K., Wells, R., Mazzotti, S., Hyndman, R.D., and Sagiya, T., 2003, A revised dislocation model of interseismic deformation of the Cascadia subduction zone. *Journal of Geophysical Research*, 108(B1), 2026. doi:10.1029/2001JB001227.

Wang, P.-L., Engelhart, S.E., Wang, K., Hawkes, A.D., Horton, B.P., Nelson, A.R., Witter, R.C., 2013, Heterogeneous rupture in the great Cascadia earthquake of 1700 inferred from coastal subsidence estimates. *Journal of Geophysical Research*. 118, 1–14. doi:10.1002/jgrb.50101.

Wilson, A. and Ma, S., 2021, Wedge plasticity and fully coupled simulations of dynamic rupture and tsunami in the Cascadia subduction zone. *Journal of Geophysical Research: Solid Earth*, 126, e2020JB021627. doi:10.1029/2020JB021627

Witter, R.C., Zhang, Y., Wang, K., Priest, G.R., Goldfinger, C., Stimely, L.L., English, J.T., and Ferro, P.A., 2011, Simulating Tsunami Inundation at Bandon, Coos County, Oregon, Using Hypothetical Cascadia and Alaska Earthquake Scenarios. *Oregon Department of Geology and Mineral Industries Special Paper* 43, 117(B10), 57 p. doi:10.1029/2012JB009404

Witter, R.C., Zhang, Y., Wang, K., Priest, G.R., Goldfinger, C., Stimely, L.L., English, J.T., and Ferro, P.A., 2013, Simulated tsunami inundation for a range of Cascadia megathrust earthquake scenarios at Bandon, Oregon, USA. *Geosphere*, 9(6), 1-21.

Zhu, Y., Wang, K., Sun, T., Carvajal, M., Luo, H., *in review*, A systematic study of dislocation modelling of megathrust tsunami sources.

10.0 APPENDIX A

Cascadia Powell Center Tsunami Sources Working Group, May 9-13, 2022 Participants

Project PI's and working group core:
Stephanie Ross (U.S. Geological Survey, Working Group Coordinator)
Marie Eble (U.S. National Oceanic and Atmospheric Administration, retired)
Christodoulos Kyriakopoulos (University of Memphis, Working Group Fellow)
Patrick Lynett (University of Southern California)
Dmitry Nicolsky (University of Alaska, Fairbanks; at this meeting, replaced by B. Salisbury)
Kenny Ryan (Air Force Research Laboratory)
Hong Kie Thio (AECOM)
Rick Wilson (California Geological Survey, participating remotely)
Other Participants, in person:
Jon Allan (Oregon Dept. of Geology and Mineral Industries, M-W in person, F remote)
Corina Allen (Washington Geological Survey)
Nic Arcos (US Nat. Oceanic & Atmos. Admin., M only)
Carrie Garrison-Laney (Washington Sea Grant Univ. of Washington, M-T)
Chris Goldfinger (Oregon State University)
Alex Hatem (US Geological Survey)
Kirstie Haynie (US Geological Survey, M-W)
Harvey Kelsey (Humboldt State University)
Ben Mason (US Geological Survey)
Jay Patton (California Geological Survey)
Mark Petersen (US Geological Survey, W only)
Peter Powers (US Geological Survey, M only)
Kelin Wang (Geological Survey of Canada)
Rob Witter (US Geological Survey)
Participating Remotely:
Steve Angster (US Geological Survey)
Rui Chen (California Geological Survey)
Alex Dolcimascolo (Washington State Department of Natural Resources)
Daniel Eungard (WA DNR Washington Geological Survey)
Art Frankel (US Geological Survey)
Eric Geist (US Geological Survey)
Joan Gomberg (US Geological Survey)
Ruth Harris (US Geological Survey)
Pat McCrory (US Geological Survey, emerita)
David Oglesby (U.C. Riverside, W 10-1, 2-4; R 12-4 pm)
George Priest (Virginia Institute of Marine Science)
Barrett Salisbury (Alaska Div. of Geological and Geophysical Surveys)
Lydia Staisch (US Geological Survey, T-F, part of M)
Janet Watt (US Geological Survey; leave T and R at 4 pm)
Stu Weinstein (US Nat. Oceanic and Atmos. Admin.)
Ray Weldon (University of Oregon; Not avail. T 10-12, W 1:30-2:30, R 1:30-3:30)
Erin Wirth (Moriarty) (US Geological Survey)
Baoning Wu (University of Southern California)
Potentially participating remotely, but scheduling conflicts will minimize it:
Alan Nelson (US Geological Survey, emeritus)
Brian Sherrod (US Geological Survey)